Advanced Functional Materials

ADVANCED FUNCTIONAL MATERIALS
www.afm-journal.de

RESEARCH ARTICLE OPEN ACCESS

Ultrasmall Platinum Nanoparticles for Radiation-Enhanced Cancer Therapy

Miguel Encinas-Gimenez[1,2,3,4] | Jose I. Garcia-Peiro[1,2,3,4] | Jose L. Hueso[1,2,3,4,5] | Eduardo Caleiras[6] | Laura Notario[7] | Felipe Hornos[8] | Pilar Martin-Duque[3,9] | Antonio De la Vieja[7] | Jesus Santamaria[1,2,3,4]

[1]Instituto de Nanociencia y Materiales de Aragon (INMA), CSIC-Universidad de Zaragoza, Zaragoza, Spain | [2]Department of Chemical and Environmental Engineering, University of Zaragoza, Zaragoza, Spain | [3]Networking Research Center in Biomaterials, Bioengineering and Nanomedicine (CIBER-BBN), Madrid, Spain | [4]Instituto de Investigación Sanitaria (IIS) de Aragón, Zaragoza, Spain | [5]Escuela Politécnica Superior, U. Zaragoza, Huesca, Spain | [6]Pathology Department, Centro Nacional de Investigaciones Oncológicas (CNIO), C. de Melchor Fernández Almagro, Madrid, Spain | [7]Endocrine Tumors Unit, Functional Unit of Research in Chronic Diseases, Instituto de Salud Carlos III, Madrid, Spain | [8]Instituto de Investigación, Desarrollo e Innovación en Biotecnología Sanitaria de Elche (IDiBE), Universidad Miguel Hernández, Elche, Spain | [9]Nanomedicine and Nanotherapies Unit, Department of Development of Advanced Drugs and Therapies (DDMTAs), Instituto de Salud Carlos III, Madrid, Spain

Correspondence: Antonio De la Vieja (adelavieja@isciii.es) | Jesus Santamaria (jesus.santamaria@unizar.es)

Received: 4 March 2026 | **Revised:** 27 March 2026 | **Accepted:** 27 March 2026

Keywords: catalysis | DNA damage | nanomaterials | platinum | radiotherapy

ABSTRACT

Despite decades of intense research, cancer remains a major global health challenge, with a clear need for new and more efficient therapies. Among emerging approaches, high atomic number (Z) nanomaterials capable of modulating the interaction between radiation and matter have attracted growing interest as radiotherapy enhancers. In this work, ultra-small Platinum-based nanoparticles with a metallic core diameter of 2–3 nm were synthesized from H_2PtCl_6 using polyvinylpyrrolidone as stabilizer. This nanomaterial exhibits low acute toxicity, catalase-like activity and enhances DNA damage under pre-clinical X-ray irradiation, increasing the antitumoral effect of X-ray alone. *In* vitro and in vivo studies, including intratumoral and intravenous administration, demonstrate improved tumor control and prolonged survival without detectable systemic toxicity under the tested conditions, establishing ultra-small Pt-nanoparticles as efficient materials for radiotherapy enhancement.

1 | Introduction

Cancer remains a major global health issue, with almost 20 million new cases in 2022 and 9.7 million cancer-related deaths worldwide. By 2050, newly diagnosed cancer cases are expected to rise to 33 million and cancer-related deaths to 18.2 million [1]. Current treatments present a set of drawbacks that limit their efficiency and application. Thus, the main challenge in classic antitumoral therapies, such as chemotherapy (CT) or radiotherapy (RT), is the lack of specificity toward the tumor [2], causing devastating side effects [3]. On the other hand, surgical excision is not always possible, and when carried out, it usually involves the elimination of a certain degree of healthy tissue to ensure the success of the procedure [4]. Clearly, new and more effective antitumoral therapies are required.

However, CT and RT are well-established and widely used treatments that have proven their efficiency in specific scenarios, despite their drawbacks. In particular, RT works by delivering high amounts of electromagnetic energy that damages DNA in the irradiated cells, with the aim of inducing death in tumoral cells. Among its different modalities, external beam therapy stands out as a local treatment, where irradiation is delivered by a machine, typically a linear accelerator [5, 6]. Although noninvasive and easy to administer, important limitations of RT include the development of radio-resistance by some kinds of

cells, as well as the low absorption of radiation energy by the tumoral tissue [4, 7, 8], since soft tissues usually present a lower absorption rate. This often makes it necessary to increase the radiation dose, which can induce toxicity in both tumoral and nearby healthy cells, since both kinds of cells display similar mass energy absorption trends [9, 10]. In this context, a significant effort is being dedicated to improving the efficiency of external beam irradiation in order to lower the doses necessary to obtain therapeutic effects.

To this end, new radiosensitizing agents are being actively developed as co-adjuvants to RT. These agents are designed to enhance the effects of ionizing radiation, allowing for dose reduction or improved tumor control at conventional doses [11]. Radiosensitizers operate through diverse mechanisms, including the inhibition of DNA repair pathways (e.g., homologous recombination and nonhomologous end joining), enhanced local electron emission and dose deposition near high-Z nanoparticles, and alleviation of tumoral hypoxia [12–16]. Among them, second- and third-row transition metals have attracted considerable attention in this regard due to their high atomic numbers (Z), which confer advantageous radiophysical properties for RT enhancement [17]. This includes elements such as gold (Au) [18, 19], platinum (Pt) [20, 21] and Gadolinium (Gd) [22, 23]. Also, post-transition metals such as gallium (Ga) [24] have demonstrated potential as radiosensitizing agents. These materials, in general, are based on the enhancement of local energy deposition [25].

It is worth noting that two nanomaterials based on the use of high-Z atoms as radioenhancers have moved forward to clinical trials: On the one hand, NBTXR3 from Nanobiotix, consists of 50 nm spherical nanoparticles composed of hafnium oxide (HfO_2) crystallites and phosphate groups, which act as radioenhancers thanks to the high Z number of hafnium ($Z = 72$) [26–28]. This treatment is currently under phase 3 clinical trial for the treatment of locally-advanced head and neck squamous cell carcinoma, among others [29]. On the other hand, AGuIX is a gadolinium oxide-based nanoparticle with a polysiloxane shell and a hydrodynamic diameter of 3 nm ($Z = 64$ for Gd) [22] that has been demonstrated to passively reach the tumors in rodent cancer models, displaying no overall toxicity thanks to renal clearance, and efficiently exerting its antitumoral effect, when activated by X-ray irradiation [30]. Currently, it has reached a phase I/II clinical trial as an RT enhancement plus concomitant Temozolomide for treatment of newly diagnosed glioblastoma [31], and a phase II clinical trial as a combined treatment with stereotactic radiation for management of brain metastases [32].

Among the named materials, platinum (Pt), in particular, holds a prominent position due to its long-standing clinical application in oncology as cisplatin and related compounds [33]. These Pt-based chemotherapeutics have been extensively characterized and are widely utilized in CT, yet the dose at which they can be administered is limited by their systemic toxicity [2]. Instead, nanoparticulate formulations of platinum offer a compelling alternative, enabling a reduction in toxicity and improved biocompatibility [34, 35]. Furthermore, Pt nanoparticles can exhibit catalase-like activity, catalyzing the decomposition of hydrogen peroxide (H_2O_2) into molecular oxygen (O_2), thus mitigating tumor hypoxia, a major contributor to radioresistance [34]. This dual functionality, encompassing both physical dose enhancement, thanks to its high atomic number, and catalytic activity capable of alleviating hypoxia in the tumor microenvironment (TME), positions Pt-NPs as highly promising candidates for synergistic RT augmentation.

However, most Pt-NPs employed to date display relatively large sizes, with diameters typically above 20 nm, either due to substantial particle growth during synthesis [36] or as a consequence of being embedded in bulky support matrices [34, 37]. A large particle size is usually considered a disadvantage as it reduces mobility and hinder tumor penetration. Also, it often results in suboptimal pharmacokinetics, prolonged tissue retention, and elevated risk of long-term toxicity [34, 38, 39]. Moreover, larger NPs exhibit reduced surface-to-volume ratios, potentially diminishing both their energy deposition efficiency (related to Auger electrons) [14] and their catalytic activity [34]. As shown by Loscertales and coworkers working with Au [40], smaller metallic NPs show a larger radiosensitizing effect than their larger counterparts. Finally, and perhaps most importantly, larger Pt-NPs cannot undergo renal filtration and urinary excretion, and this favors longer-term accumulation after systemic administration. It should be noted, however, that potential renal elimination cannot be inferred from size alone: renal excretion of ultrasmall metal nanostructures has been reported to be variable depending on NP nature and surface chemistry [41], and therefore, biodistribution and clearance must be experimentally validated for each formulation. Consistent with the size-dependence of nanoparticle biodistribution, Yang et al. provided one of the first PET-quantified in vivo pharmacokinetic studies of radio-enhancer platinum nanoparticles (ca. 9 nm) and nanoflowers (ca. 35 nm), reporting peak tumor accumulation at ~24 h and sustained retention [42]. To address these limitations, in the present work we have developed ultrasmall Pt-NPs using polyvinylpyrrolidone (PVP) as stabilizer, giving a NPs population with metallic core diameter of 2.6 ± 1.1 nm measured by TEM and in any case with diameters below 6 nm, within the commonly cited glomerular filtration size range [43], although as stated, specific validation for each formulation is required. For clarity, throughout this manuscript, "nanoparticle size" refers to the TEM-measured metallic core diameter unless otherwise stated.

In this regard, a broad range of Pt-based materials have been developed as nanoparticles intended to enhance X-ray effects without other irradiation sources or co-therapy, as summarized in Table S1. However, the number of works carried out with ultrasmall nanoparticles is quite scarce. To the best of our knowledge, only the studies by George et al. [44] and Pagáčová et al. [45] have previously proposed the use of ultra-small NPs (< 6 nm in diameter) based on Pt for the enhancement of X-ray therapy in tumoral cells, although they were not tested in vivo. Other works have likewise performed complete studies of ultra-small Pt-NPs [46], including their use in vivo [47]; however, although their TEM-measured metallic core diameters were below 6 nm, the presence of organic coatings increased their hydrodynamic sizes relative to the core.

In this work, we present a comprehensive investigation of ultrasmall Pt nanoparticles with a TEM core diameter of 2.6 ± 1.1 nm (Pt-NPs) and their capacity to enhance radiotherapeutic efficacy via both radiophysical and biochemical mechanisms, demonstrating low toxicity in several conditions and cell lines,

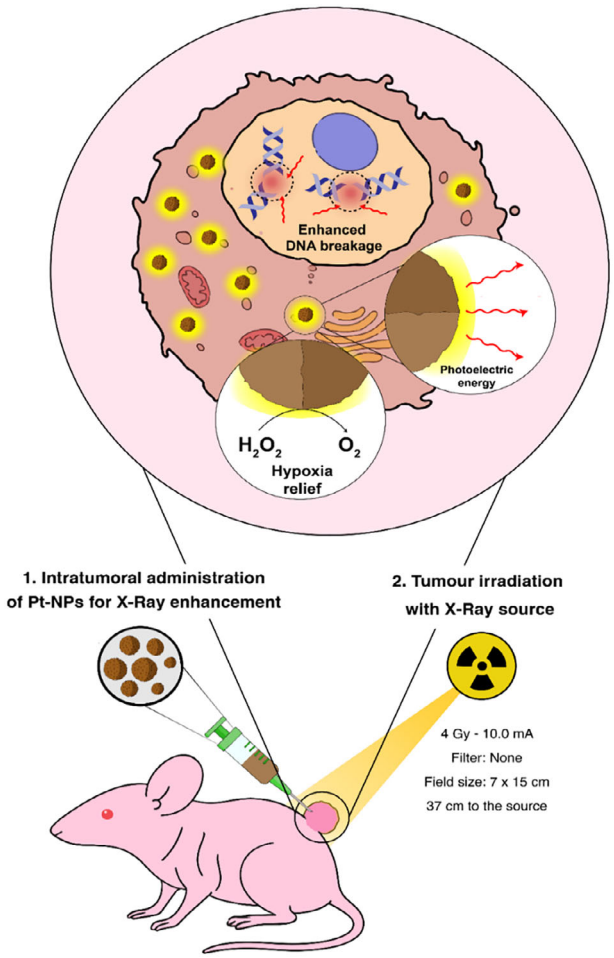

FIGURE 1 | Pt-NPs as radiosensitizers. Schematic representation of the therapeutic strategy followed by ultrasmall Pt-NPs administration, as well as the cellular effects when Pt-NPs are combined with x-rays.

as well as enhanced toxicity and DNA damage when combined with pre-clinical X-ray therapy. Following the in vitro study, their capability to enhance radiation effects was assessed in vivo with intratumoral injection of Pt NPs, demonstrating an excellent performance in the reduction of xenograft tumors from two different tumoral cell lines. Finally, the therapeutic performance and systemic safety of systemically (IV injection) administered Pt-NPs in combination with localized irradiation were also assessed in vivo, thereby complementing intratumoral administration studies and providing a more clinically realistic assessment of radiosensitization. The experimental procedure for in vivo irradiation, as well as the proposed mechanism of action for Pt-NPs, is displayed in Figure 1.

2 | Results and Discussion

2.1 | Synthesis and Characterization of Pt-NPs

The Pt-NPs were synthesized via a solvothermal method using H_2PtCl_6 as Pt precursor and 10000-MW polyvinylpyrrolidone (PVP) as stabilizer, following the simplified visual workflow presented in Figure 2A. The reaction presumably proceeds via a two-step reduction pathway, where the Pt (IV) precursor is reduced to a Pt (II) intermediate during an induction period, followed by a complete reduction to metallic Pt(0) species, with ethanol playing a dual role as a co-solvent and a reducing agent. This redox process is coupled with the oxidation of ethanol into acetaldehyde, promoting the transformation of the metallic precursors until the accumulation of Pt(0) atoms reaches the concentration necessary for nucleation. The role of PVP as stabilizer is presented in Figure S1. PVP attaches to platinum surfaces via chemisorption of the carbonyl oxygen, regulating particle growth and preventing their aggregation (Figure S1A) [48]. The nascent Pt^0 clusters are capped by PVP (MW 10 000), which adsorb on the metallic surface and sterically stabilizes the nuclei, suppressing ripening and aggregation (Figures S1B,C and S2), leading to PVP-stabilized ultrasmall Pt NPs. In our synthesis, the PVP:Pt mass ratio in the reaction mixture was approximately 5:1 (w/w), with a significant excess of polymer relative to metal. While this PVP corona is expected to increase the hydrodynamic diameter, with 2–3 nm core particles, the final size was still under the range of conventional sizing techniques such as dynamic light scattering (DLS) or nanoparticle tracking analysis (NTA). Indeed, as expected, size measurements on our Pt NP dispersions did not give any reliable readings.

This limitation is consistent with the presence of ultrasmall metallic nanoclusters whose scattering cross-section falls below the reliable detection range of conventional DLS/NTA methods. For this reason, we report only the TEM-measured metallic core size as the most accurate descriptor of the inorganic core, and we interpret the material as PVP-stabilized Pt nano-cores rather than "naked" Pt, even though the low-Z PVP corona is not visible in Z-contrast imaging.

Transmission Electron Microscopy (TEM) analysis (Figure 2B) confirmed ultrasmall cores of Pt-NPs with a size around 2–3 nm (2.6 ± 1.1 nm) with crystalline facets associated with cubic Pt (Figure 2C). HAADF-STEM confirms isolated ~2–3 nm Pt cores (Figure S1B,C). X-ray diffraction analysis (XRD) further confirmed the crystalline phase of Pt with a face-centered cubic structure (Figure 2D). X-ray photoemission analysis of the Pt 4f region also confirmed the metallic nature of Pt species with binding energies of 71 and 74.3 eV for the Pt $4f_{7/2}$ and Pt $4f_{5/2}$ regions, respectively (Figure 2E) [35, 36, 49]. In this case, the catalase-like activity was tested by monitoring the evolution of dissolved O_2 levels following successive injections of a H_2O_2 solution. The Pt-NPs were very active in generating oxygen (O_2) from hydrogen peroxide (H_2O_2), as can be seen in Figure 2F. However, this catalytic activity was demonstrated under cell-free conditions. To exert their catalase-like activity inside cells, Pt-NPs would have to be internalized and maintain their catalytic activity after the process. These aspects have not been investigated in this work. Finally, these particles showed high colloidal stability over time, with no significant changes after being stored at 4°C for 4 months (Figure S2).

2.2 | In Vitro Cytotoxicity of Pt-NPs

The in vitro cytotoxicity of the Pt-NPs was assessed using two tumoral cell lines (U-251 MG and HeLa), and a nontumorigenic cell line (human placenta mesenchymal stem cells, hpMSCs). These cell lines were incubated with increasing concentrations of

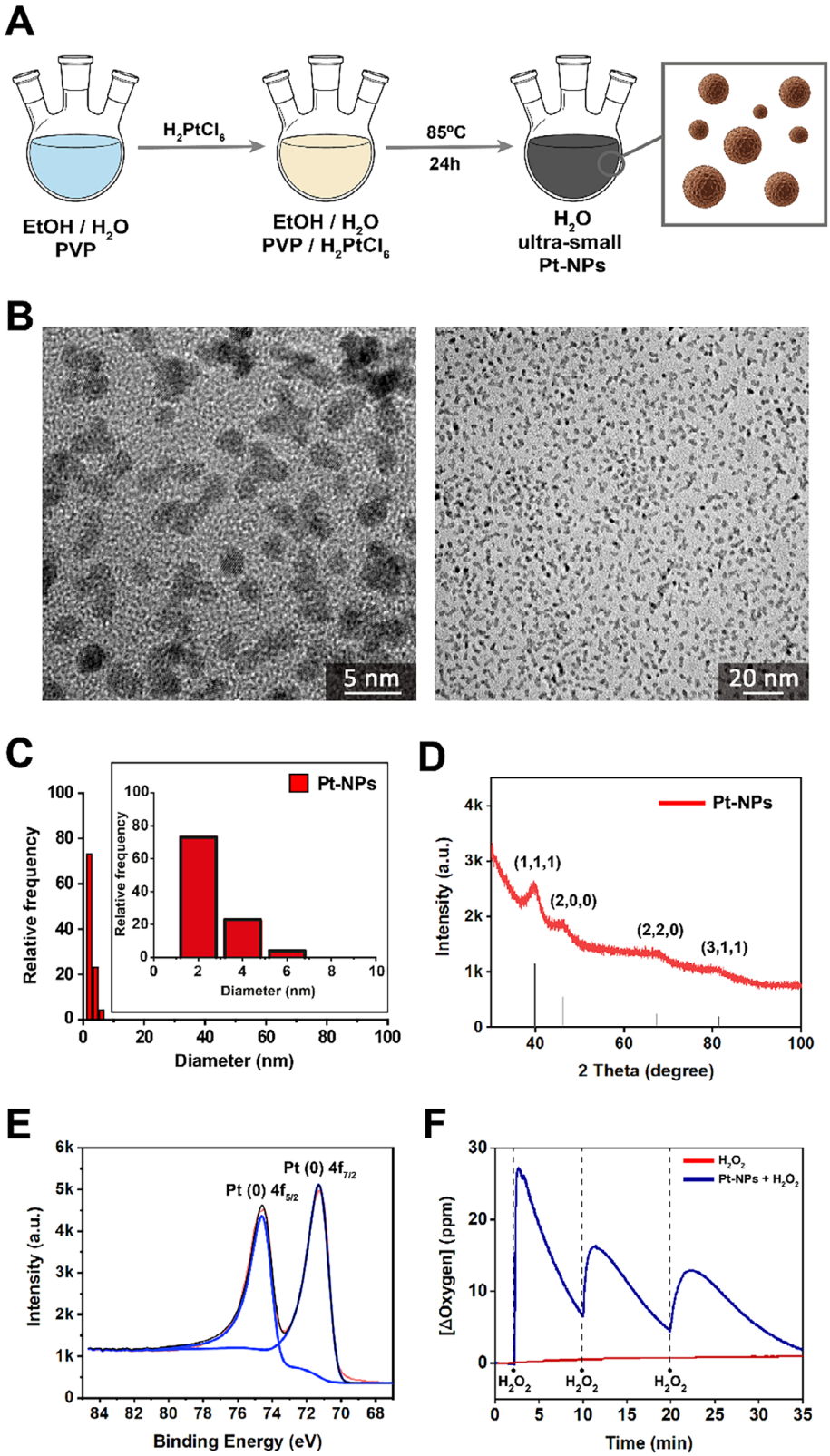

FIGURE 2 | Pt-NPs characterization. (A) Schematic workflow of Pt-NPs synthesis, indicating the main steps followed during this process. (B) Representative TEM images of a Pt-NPs stock solution in distilled water (dH_2O), under two different magnifications. (C) Histogram representing the relative frequencies of the different diameters for Pt-NPs, measured with ImageJ software from TEM images. (D) XRD and (E) XPS analysis of a stock solution of Pt-NPs. (F) Oxygen generation capacity of Pt-NPs in the presence of H_2O_2 across time. 2 mL of H_2O_2 (1 mM) were initially added, then 0.05 mL of H_2O_2 (20 mM) was subsequently added at 10 and 20 min, as indicated in the graphic.

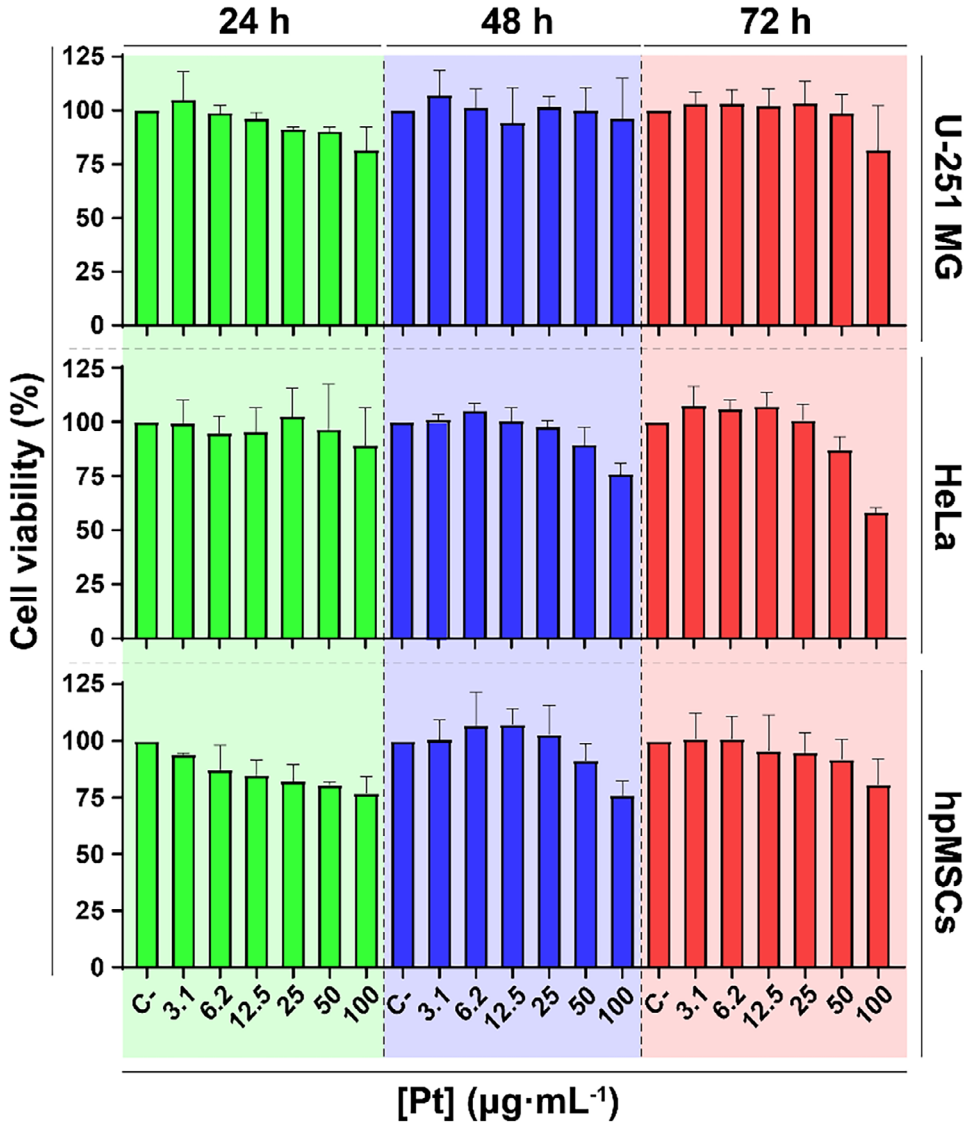

FIGURE 3 | Cell viability after Pt-NPs administration. Viability of tumoral (U-251 MG, HeLa) and nontumoral (hpMSCs) cell lines after treatment with increasing concentrations (from 3.1 to 100 μg·mL^{-1}) of Pt-NPs for 24, 48, and 72 h. Data are shown as mean ± SD ($n = 3$).

Pt-NPs (ranging from 3.1 to 100 μg·mL^{-1}) and cell viability was determined after 24, 48, and 72 h based on metabolic activity, normalized to untreated controls. Overall, results indicated a low acute cytotoxicity of the Pt-NPs across all tested cell lines and timespans (Figure 3). Notably, HeLa cells exhibited increased sensitivity after 72 h of exposure, representing the only condition in which cell viability dropped below 70% at the highest concentration used.

Considering the results of the cell viability assay, 100 μg·mL^{-1} was the Pt-NPs concentration selected for further experiments, since all cells (except for HeLa after 72 h) presented a good response to this concentration, and even HeLa cells did not display a dramatic viability reduction. Especially, nontumoral cells (hpMSCs) displayed a good viability at this concentration. In addition, as it will be later explained, the optimal internalization time was established at 24 h, a time at which cell viability was above 75% in all cases. These findings are consistent with previous viability studies conducted at similar concentrations, both in systems containing Pt as the sole metallic component [20, 50], as well as in materials that combine Pt with other metals [7, 51, 52].

2.3 | Internalization of Pt-NPs in Cells

Although the cell viability assays yielded favorable results, it was essential to quantitatively determine NPs internalization to ascertain whether the high viability values observed resulted from actually low toxicity or from insufficient internalization of Pt-NPs. To evaluate nanoparticle internalization, cells were incubated with 100 μg·mL^{-1} Pt-NPs using the same time intervals as in the viability assays. Following incubation, noninternalized Pt-NPs were removed by PBS washing, and cells were imaged by confocal microscopy and later digested for quantitative Pt analysis. Confocal images shown in Figure 4 and Figures S3–S5 should be interpreted as qualitative localization of aggregates and cannot yield quantitative uptake measurements, as its resolution does not allow to observe well-dispersed Pt NPs inside cells.

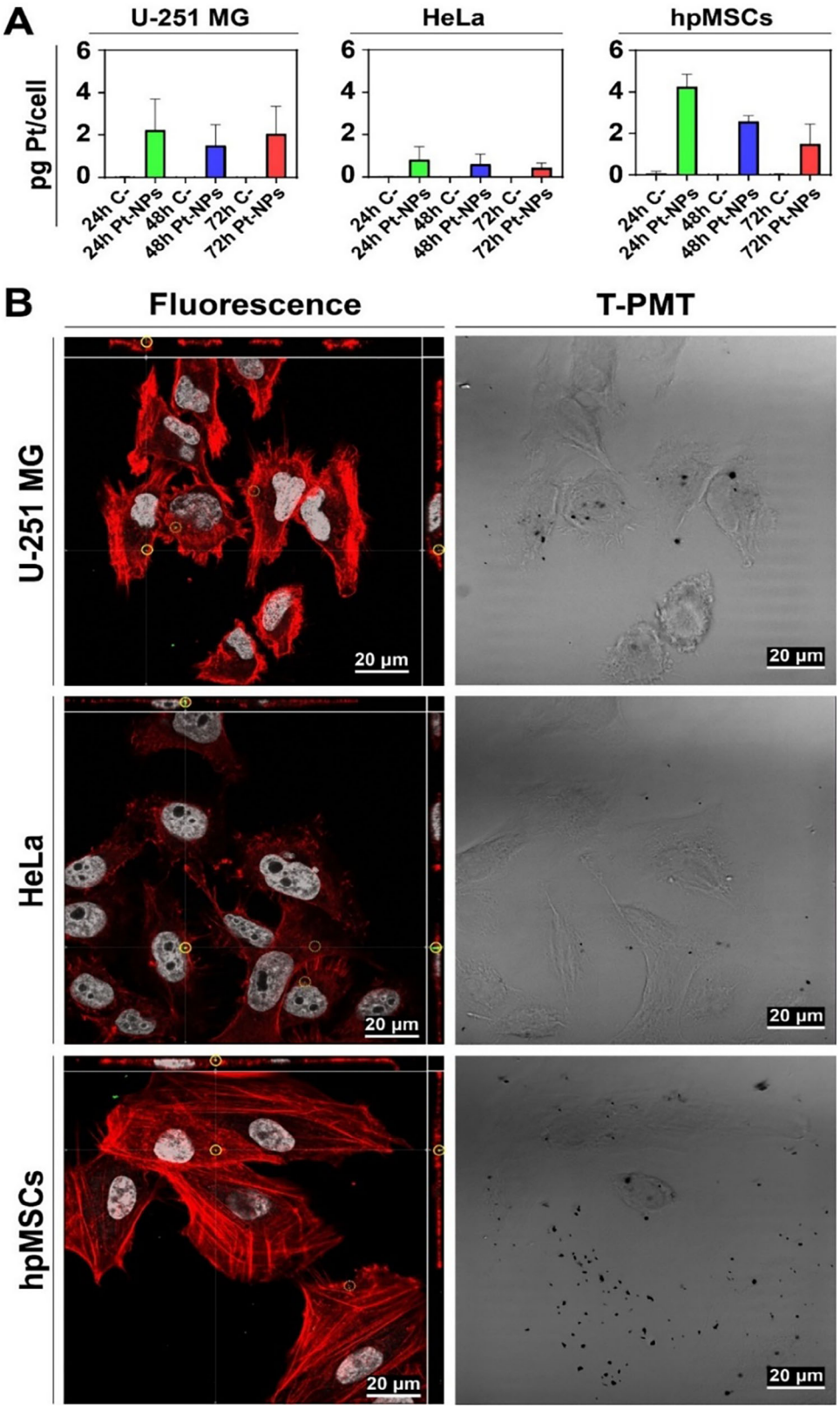

FIGURE 4 | Internalization of Pt-NPs. (A) Quantification of Pt internalized in different cell lines after incubation with 100 µg·mL^{-1} of Pt-NPs during 24, 48, and 72 h. Data obtained from MP-AES elemental analysis are shown as mean ± SD ($n = 3$). (B) Confocal microscopy images of Pt-NPs internalization in several cell lines after the treatment. A few bright green dots (left column) can be spotted, corresponding to the metallic reflection of Pt-NPs aggregates. Also, the use of a photomultiplier for transmitted light (T-PMT) allows the detection of clusters of nanoparticles by contrast, appearing as black dots (right column). Detector gain was 600 for Channel 1 (red, phalloidin) and Channel 2 (gray, DAPI), 680 for Channel 3 (green, reflection), and 440 for Channel 4 (T-PMT).

Quantification by MP-AES constitutes the primary evidence of Pt-NPs uptake, whereas reflection/T-PMT confocal imaging provides qualitative support only. Because individual 2–3 nm Pt-NPs are below the optical resolution limit, this imaging modality detects only clustered or highly reflective Pt-containing assemblies. Therefore, these images support intracellular localization of detectable aggregates, but cannot be interpreted as indication of Pt-NPs distribution inside the cells. Both U-251 MG and hpMSCs exhibited evident uptake of Pt-NPs at all times studied. Notably, HeLa cells exhibited the lowest level of particle internalization among the cell lines tested (Figure 4A). These results are consistent with the study by Encabo-Berzosa et al., who reported reduced internalization of a metallic nanomaterial in HeLa cells compared to mesenchymal stem cells [53]. Also, the maximum nanoparticle content was observed at 24 h in all cell lines for our Pt-NPs.

Confocal microscopy was therefore used to confirm intracellular internalization, and rule out other phenomena, such as surface adhesion on the outer cellular membrane. To this end, cells were incubated *de novo* with Pt-NPs for 24 h and examined via confocal microscopy to visualize intracellular nanoparticle aggregates. After exposure, cells were extensively washed to remove noninternalized material, fixed, and stained. Then, a Z-Stack image was obtained, compressing all the slices between the top point and the bottom point of the cell. Figure 4B and Figures S3–S5 show a representative example of these Z-slices for each cell line, with nuclei stained in grey (DAPI) and actin fibers in red (Phalloidin-Alexa Fluor 488, see Experimental Section for details). Nanoparticle aggregates (as stated, individual 2–3 nm particles are far below the resolution limit of the confocal microscope), detected by reflection of the incident light, can be spotted as green dots. These slices are accompanied by their orthogonal projections along the *X* and *Y* axes of the image, providing a *Z*-axis cross-sectional view, helping to confirm the presence of the nanoparticle aggregates inside the cells (yellow circles). It is likely that much more Pt is present in the cell as dispersed NPs, under the resolution of the confocal microscope, as confirmed by MP-AES.

Additionally, the photomultiplier for transmitted light (T-PMT) of the confocal microscope revealed nanoparticle aggregates as high contrast black dots in bright field images (Figure 4B; S3–S5). Although this modality does not confirm the intracellular location of Pt-NPs, it provides complementary information regarding aggregate distribution. In contrast, when the same procedure was applied to cells that did not undergo any treatment with nanoparticles (negative control), the aggregates were absent from both fluorescence images and transmitted-light images (Figure S6). Thus, quantitative MP-AES measurements together with orthogonal confocal projections provide complementary evidence of nanoparticle internalization, combining elemental quantification with spatial localization of aggregates.

As previously noted, and as summarized in Table S1, research works dealing with ultra-small Pt-NPs as radiosentitizers are scarce. We highlight the works by George et al. [44], Pagáčová et al. [45], Salado-Leza et al. [46], and Yaray et al. [54]. Also, taking into account that size is one of the main factors affecting cellular uptake, it is hard to make direct comparisons regarding the internalization efficiency among different Pt nanoparticles. Previous studies indicate that Pt-NPs may display different subcellular distributions depending on nanoparticle design and cell type, but localization in the nucleus is not required to observe enhanced radiosensitization. Thus, in HeLa cells, radiosensitization has been reported for Pt-based nanomaterials predominantly localized in the cytoplasm rather than in the nucleus [46, 55], whereas for ultrasmall 2 nm Pt-NPs, a measurable intranuclear platinum fraction has been described in HepG2 cells [56]. It should also be noted that not all Pt NPs produce the same outcome under irradiation. Some studies have shown weaker or absent enhancement under other cellular models and irradiation settings, underscoring that platinum-based radio-enhancement is strongly model- and condition-dependent [57]. In this work, data clearly support cellular uptake and intracellular localization of detectable Pt-containing aggregates. While nuclear internalization of a fraction of Pt NPs also seems likely given their size, this was not determined in this case. Several studies have reported internalization values for different metal nanoparticles and can be used for comparison. Thus, internalization of Au@Pt nanodendrites (~30 nm) [58] and Pt-prodrug@Fe_3O_4 NPs (~20 nm) [59] has been investigated in 4T1 cells. Reported values of ~90 ng Pt/10^4 cells in both studies (after 24 and 2 h, respectively) show a higher internalization rate than the values herein observed for U-251 MG and hpMSCs (22.4 and 42.4 ng Pt/10^4 cells after 24 h, respectively). Regarding HeLa cells, Liang et al. reported ~950 fg Au / cell after 30 min incubation with the highest studied concentration of modified Au nanoclusters [60]. This value is close to the Pt content measured in our study with HeLa cells after 24 h (820.1 fg Pt/cell). This latter comparison might be relevant since the clusters were smaller than 2 nm.

2.4 | Combined Effect of Pt-NPs and X-Ray Irradiation in Tumoral Cells Lines

2.4.1 | Pt-NPs Radiosensitizing Effect

Following the assessment of the effects of Pt-NPs incubation alone, the next step involved evaluating their impact under X-ray irradiation in cell culture. To this end, an initial cytotoxicity assay was conducted to evaluate the Pt-NPs' ability to enhance the effects of X-ray exposure. This enhancement would be consistent with high-Z-mediated dose amplification and short-range secondary electron emission, mechanisms widely recognized as primary contributors to nanoparticle-mediated radiosensitization.

RT alone has reportedly been able to reduce cell viability in different tumoral cell lines, such as lung cancer [20], murine breast cancer [50, 52] or hypopharyngeal cancer [61], showing variable effects depending on the cell line. In this regard, HeLa (cervical adenocarcinoma) [60, 61] and U-251 MG (malignant glioblastoma) [62] cells, both used in this study, exhibit a dose-dependent response to X-ray treatment. Clinically, the application of RT differs between cervical cancer and glioblastoma. RT plays a central role in the clinical management of cervical cancer [63]. In contrast, newly-diagnosed glioblastoma is typically treated with surgical resection followed by RT and temozolomide CT, however, median survival from initial diagnosis is less than 15 months [64]. In any case, it should be noted that the equipment

herein employed (Faxitron Multirad 225) works in the energy range of kV, whereas according to the I.A.E.A. Human Health Report of 2022, 6 MV is currently the commonest choice of energy for single energy standard linear accelerators or robotic RT [65]. Indeed, the range of MV is often found in clinics for different types of tumors: glioblastoma [66] or glioma [67], and cervix carcinoma [68, 69].

Prior in vitro studies with these two cell lines demonstrated that irradiation doses below 6 Gy did not induce substantial cytotoxicity [60–62]. These findings support the rationale to use Pt-NPs to enhance RT effects while reducing X-ray irradiation dosing and minimizing damage to healthy tissues. To investigate whether Pt-NPs administration could significantly amplify X-ray-induced cytotoxicity, cells were treated with Pt-NPs (100 $\mu g \cdot mL^{-1}$) for 24 h, then noninternalized Pt-NPs were rinsed with PBS washing, and cells were subsequently exposed to increasing X-ray doses ranging from 0 to 4 Gy, in the irradiation machine (Figure S7). This equipment incorporates a built-in dosimeter, an ion chamber located in the center of the turntable, which communicates to a dosimeter module, allowing the measurement and handling of the irradiation rates and doses. Cell viability was determined by counting adherent cells 7 days after the irradiation. Results showed that, in both cell lines, Pt-NPs addition led to increased cytotoxicity compared to X-ray irradiation alone (Figure 5A).

In the case of HeLa cells, despite moderate effects, the results are notable given the low Pt-NPs internalization observed in these cells (Figure 5A). In U-251 MG cells, radiation alone already induced a strong cytotoxic effect, which was, however, notably increased by Pt-NPs treatment (Figure 5A). This enhancement is generally expected for Pt-based nanoparticles, as shown in previous studies [20, 50]. However, the increase observed in this case is especially noteworthy, taking into account the ultrasmall size of the Pt-NPs used, which resulted in a moderate internalization (22.4, 8.2, and 42.4 ng $Pt/10^4$ cells after 24 h for U-251 MG, HeLa, and hpMSCs, respectively). Next, the mechanism of action was further investigated using a 4 Gy dose in subsequent experiments.

The gap between both curves corresponding to U-251 MG cells in Figure 5A indicates that Pt NPs already have a moderate cytotoxic effect on these cells. This was not detected in the cytotoxicity experiments of Figure 3, for these experiments were carried out for a maximum time of 72 h. However, for Figure 5A, data were taken 7 days after irradiation (i.e., 8 days after initial exposure to Pt-NPs), and a delayed cytotoxicity appears. In contrast, for HeLa cells, this effect was negligible. To distinguish this basal cytotoxic effect from actual radio sensitization, we performed an additional analysis in which each treatment group was normalized to its own baseline of 0 Gy (0 Gy/0 $\mu g \cdot mL^{-1}$ for the control curve and 0 Gy/100 $\mu g \cdot mL^{-1}$ for the Pt-NPs curve), and compared the dose response slopes using linear regression (Figure S8). While the fitting gives a slightly higher slope for the Pt-NPs treated cells, the differences for U-251 MG were not statistically significant, indicating that most of the total loss of viability in this line reflects the combination of late Pt-NP cytostatic and irradiation. In contrast, in HeLa cells, the slopes were significantly different ($p = 0.0397$), indicating that Pt-NPs significantly potentiate the cytotoxic effect of X-ray irradiation in this cell line.

To quantitatively compare the enhancement of X-ray cytotoxicity by Pt-NPs, we calculated a dose-modifying ratio at 50% viability, DMR_50(viability). This parameter is defined as the ratio between the radiation dose required to reach ~50% viability in the absence of Pt-NPs and the dose required to reach the same viability after Pt-NPs incubation. Thus, DMR_50(viability) > 1 indicates that the nanoparticles allow achieving the same cytotoxic effect with a lower radiation dose, consistent with radio sensitization. This approach is conceptually analogous to the "dose-modifying ratio at 50% survival" and "dose-modifying factor at SF_50" commonly used in nanoparticle radio sensitization studies [70, 71], adapted here to our viability-based assay rather than clonogenic survival. We observed DMR_50(viability) > 1 for both U-251 MG and HeLa cells, even after correcting for baseline Pt-NPs effects, supporting that Pt-NPs act as enhancers of radiation effects in both models. Full methodology, normalization strategy, and numerical values are provided in Methods S2.

2.4.2 | Effects on γH2AX Histone and 53BP1 Expression

DNA damage induced by X-ray irradiation usually manifests as double-strand breaks (DSBs), which can result from ionizing radiation or cytotoxic agents, causing lethal disruptions in DNA strands [72]. The presence of this kind of damage triggers two repair systems in DNA, named as homologous recombination (HR) and nonhomologous end joining (NHEJ) [73, 74]. One of the cellular responses to DSBs involves the recruitment and activation of the ataxia-telangiectasia mutated (ATM) kinase by the sensor complex, which leads to the phosphorylation of histone H2AX on serine 139, resulting in γH2AX, which promotes DNA damage signal amplification and DSBs repair through HR [75, 76]. The presence of this phosphorylated histone in the DSB sites is required for the downstream accumulation of several DNA-damage response (DDR) proteins. Among them, p53-binding protein 1 (53BP1) plays a key role in promoting DNA repair by NHEJ, maintaining the balance between the two major repair systems [73–76].

The expression of γH2AX histone was evaluated by immunocytochemistry, since its phosphorylated form appears as nuclear fluorescent "*foci*," corresponding to the DSB sites. The quantification of γH2AX nuclear foci is broadly accepted as a biomarker of DNA damage in a living cell [76, 77], and correlates with an increase in impaired proliferation or cell death.

To assess the effect of irradiation on DNA damage, cells were irradiated at 4 Gy either in the presence or absence of Pt-NPs, then were fixed for immunocytochemistry 60 and 120 min after X-ray administration. These time points were selected based on previous reports showing that the appearance of this phosphorylated histone occurs shortly after the DNA damage event (in this case, ionizing radiation). For instance, Gaudreau-Lapierre et al. reported that γH2AX signals should emerge at 5 min and persist up to 3–4 h after the DNA damage takes place [78]. Similarly, Martinez-Pastor et al. detected foci indicative of

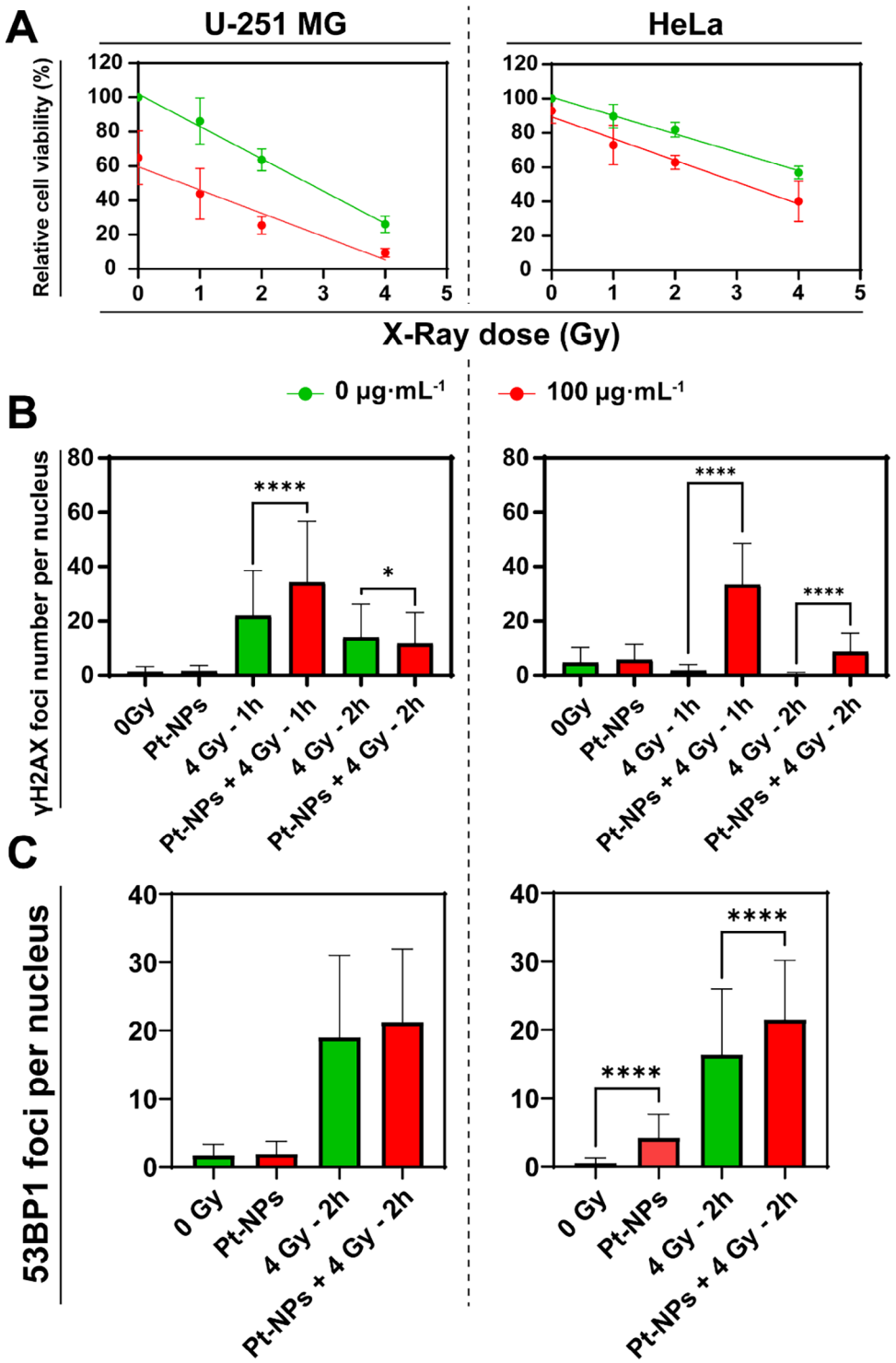

FIGURE 5 | X-ray cytotoxicity enhancement of Pt-NPs. (A) Effect of increasing doses of X-ray on the viability of U-251 MG and HeLa cells, in the presence or absence of Pt-NPs (100 µg·mL^{-1}), incubated for 24 h. Cells counted 7 days after X-ray administration ($n = 3$). (B) Counting of γH2AX foci number for every condition at different times after irradiation. Both U-251 MG and HeLa cells were assessed (nuclei number between 188 and 335 for U-251 MG and between 250 and 469 for HeLa). (C) Counting of 53BP1 foci per cell nucleus 2 h after X-ray application, for U-251 MG and HeLa cells (*nuclei number* from 140 to 271 for U-251 MG, and from 190 to 341 for HeLa). Data are shown as mean ± SD. Statistical significance assessed by *t*-test applying Welch's correction when necessary: *$p < 0.05$, **$p < 0.01$, ***$p < 0.001$, ****$p < 0.0001$.

DNA damage 15 min after gamma irradiation, with persistence for 90 min, followed by a decrease from 6 h onward [75].

In our case, confocal imaging confirmed clear nuclear staining of γH2AX. Fluorescence signal was almost negligible in nonirradiated cells and in cells incubated with Pt-NPs alone (100 μg·mL^{-1}), then, in experiments with X-ray irradiation alone, the γH2AX signal clearly increased, rising further when the radiation dose was combined with a prior incubation with Pt-NPs (Figure 5B). The differences were highly significant ($p < 0.0001$) for HeLa cells and for U-251 MG after 1 h. These findings were corroborated by orthogonal projections of confocal images, revealing an increased number of γH2AX foci signals in both U-251 MG (Figure S9) and in HeLa cells (Figure S10) under combined treatment. Overall, these results indicate that Pt-NPs amplify DNA damage signaling following irradiation, as shown by the number of γH2AX foci present in the nuclei, especially in HeLa cells.

Similarly to the role of γH2AX, the expression of 53BP1 has been associated to an increased DNA damage. Thus, for instance, 53BP1 expression was spotted by Martinez-Pastor and coworkers 15 min after gamma irradiation, and, similar to their observations regarding γH2AX, it persisted during the first 90 min and started decreasing 6 h after gamma irradiation [75]. Given the sustained γH2AX foci expression observed with the combined treatment (1 h in U-251 MG, 2 h in HeLa), 53BP1 expression at the 2-h mark could serve as an additional indicator to validate the persistence of DNA damage, with lower foci expected for X-ray alone.

Immunocytochemistry for 53BP1 was performed in a similar way to γH2AX, using Alexa Fluor 488-conjugated secondary antibodies. Once again, images were evaluated by counting the number of 53BP1 active pixels, and the results are displayed in Figure 5C. On the one hand, the combined treatment in U-251 MG presented a tendency toward increasing the *foci* number per nucleus compared to the application of irradiation alone (yet it was not statistically significant due to the wide dispersion of data). On the other hand, 53BP1 foci significantly rose their number in HeLa cell nuclei after the combined therapy, compared to the X-ray treatment alone, 2 h after the treatment application. Representative orthogonal confocal projections support the quantitative analysis, confirming increased foci formation (Figure S11).

However, the fact that solely incubation with Pt-NPs already produced a significant increment in 53BP1 foci numbers in HeLa cells (Figure 5C) must not be overlooked, since although it was a small increase, it was significant. A small increase (though not statistically significant) could also be ascertained in Figure 5B for the Pt-NPs-treated HeLa cells in the γH2AX experiment. Both results would suggest that, specifically for this cell line, there is some DNA damage associated with the internalization of Pt-NPs. The explanation for this phenomenon is still unclear to us, although some studies have reported the increment in 53BP1 foci expression following cisplatin exposure in tumor cell lines, such as A549 [79], and SiHa [80] (a cervical carcinoma cell line). A slight, nonsignificant increase in γH2AX and 53BP1 was observed in HeLa cells after incubation with Pt@Au NPs [7], yet the thorough explanation for this phenomenon has not been previously described, to our knowledge. It seemed possible that, due to the ultrasmall size of the Pt-NPs used in this work, with an extremely high external surface to volume ratio, some Pt dissolution may take place, and in this case, the observed behavior would reflect the effect of leached Pt behaving analogously to cisplatin. In any case, the amount of Pt that could be potentially dissolved from our nanoparticles is necessarily very small (to check this, we incubated 0.2 mg of Pt-NPs for 8 h in 1 mL of cell culture medium at 37°C and the amount of leached Pt was under the MP-AES detection limit), and indeed our cell viability experiments showed that Pt-NPs treatment at the tested concentrations did not induce cytotoxicity even in HeLa cells at 24 or 48 h post-incubation.

Both proteins, γH2AX and 53BP1, have also been assessed in similar works. In the case of γH2AX, previous studies involving Pt-based nanomaterials have reported comparable results, including noticeable increases in foci per cell [20], or enhanced nuclear fluorescence intensity at early time points [50]. Besides, bimetallic Au-Pt-NPs have also shown a pronounced effect on γH2AX expression and nuclear localization [7, 52, 81]. In contrast, 53BP1 has been less frequently studied, yet there are some precedents. For instance, Jackson et al. reported a moderated increase in 53BP1 foci 24 h after 2 Gy irradiation, when Au NPs were combined with docetaxel, compared to Au NPs + X-ray alone [82]. It is also noteworthy the work by Zhang et al., who used 36 nm Pt@Au nanoparticles to induce enhanced RT effects and noticed increased γH2AX foci per cell. However, they also found that cells with the highest number of γH2AX, also displayed the lowest number of 53BP1 foci, suggesting that DSB repair was impaired by the treatment [7]. In contrast, in this work, 53BP1 and γH2AX foci count variations seemed to be highly correlated, giving strong evidence that the Pt-NPs used in this work enhance and prolong DNA damage signaling when combined with X-ray irradiation.

Finally, we performed intracellular ROS measurements to assess whether the additional loss of viability observed in the presence of Pt-NPs could be attributed simply to amplified ROS generation. Total ROS levels were quantified using the H_2DFCDA probe and plate reader detection 30 min after irradiation, and the results are shown in Figure S12. As shown, irradiation at 4 Gy produced a modest and nonsignificant upward trend in ROS in both U-251 MG and HeLa cells, while the addition of Pt-NPs did not further increase the ROS signal at this time. This does not contradict the observed increase in γH2AX and 53BP1 foci with Pt-NPs + X-rays, as ultra-small Pt-NPs are expected to increase local energy deposition and short-range electron emission under irradiation, producing highly localized DNA double-strand breaks through a Pt-mediated catalytic redox process consistent with the H_2O_2 decomposition and O_2 generation observed in cell-free assay (Figure 2F), which could contribute to oxygenation-dependent fixation of radiation-induced DNA lesions. Both effects can intensify persistent DNA damage without causing a significant increase in global ROS, since the catalytic action of Pt NPs depletes H_2O_2, one of the main contributors to ROS measurements.

From a mechanistic point of view, the radiosensitizing action of ultrasmall Pt-NPs is likely multifactorial. Pt high-Z properties can enhance local physical interactions under irradiation, while previous studies also support catalytic H_2O_2 decomposition/O_2 generation as a possible contributor to RT enhancement [20].

In the present work, the catalytic activity of the ultrasmall Pt NPs used has been clearly shown in cell-free conditions, whereas intracellular or in vivo catalytic activity was not directly measurable. It is important to note that catalysts may lose their activity in biological environments, e.g. due to poisoning by sulfur-containing molecules [83]. Therefore, the catalytic contribution should be interpreted as a likely local component of radiosensitization rather than as a demonstrated intracellular mechanism in this case.

2.5 | In Vivo Radiosensitization Performance of Pt-NPs

Encouraged by the clear potential shown by Pt-NPs to enhance the effects of X-ray irradiation and their capability to induce a higher, more enduring DNA damage, we also studied the effects of the combined treatment (Pt-NPs + RT) in vivo. For this purpose, two different xenograft tumor models were established using U-251 MG and HeLa cells in 6–10-week athymic female mice. Tumor implantation methodologies for both xenograft models have been adapted from previous works [2, 84, 85] with minor modifications (see further details in the Experimental section). To evaluate both mechanistic efficacy and translational relevance, in vivo experiments were performed using two administration strategies: intratumoral administration and intravenous delivery. Intratumoral administration was used as a mechanistic proof-of-concept to isolate intrinsic radiosensitizing capacity from delivery limitations, in a dose-controlled scenario. On the other hand, intravenous injection allows to study a more relevant therapeutic scenario of systemic administration, where only a fraction of the NPs injected reaches the tumor. Off-target deposition is likely in this case, and therefore, endpoint serum biochemistry and liver/kidney histology are reported for the IV study.

2.5.1 | Intratumoral Treatment in the U-251 MG Xenograft Model

The results of the treatment in the case of the xenograft originating from U-251 MG cells are presented in Figure 6. As depicted in Figure 6A, after subcutaneous injection of U-251 MG cells, tumors were allowed to grow for 7 days, then a single Pt-NPs intratumoral injection (100 μL, 3 $mg{\cdot}mL^{-1}$ in PBS) was administered. X-ray irradiation (4 Gy) was applied the following day (day 8) and again on day 13 (total dose: 8 Gy).

The irradiation dose used for this assay was selected taking into account other studies working with metal-based radiosensitizers that obtained significant results in the range between 4 and 12 Gy of total dose [7, 77, 86–88]. Thus, we decided to administer a total X-ray dose of 8 Gy (4 Gy x 2 days).

Regarding the quantity of Pt-NPs injected, there is considerable variability in the literature regarding the total mass of intratumorally administered nanomaterials. In some cases, the treatment was only one 50 μL injection at concentrations ranging from 1 to 3.8 $mg{\cdot}mL^{-1}$ of the nanomaterial [77, 88]. In another work, Zhang et al. administered 100 μL of the nanomaterial at a concentration of 10 $mg{\cdot}kg^{-1}$ [7]. Also, Yong et al. treated the mice with 20 μL injections of the nanomaterial at 2 $mg{\cdot}mL^{-1}$, improving the therapeutic effectiveness [86]. In our case, we decided to carry out only one injection of Pt-NPs (100 μL at 3 $mg{\cdot}mL^{-1}$). In spite of this, the employed concentration was still a slightly higher quantity of nanomaterial compared to other related works. However, the low toxicity that Pt-NPs showed in vitro (although it was moderately increased 8 days after NP incubation in U-251 MG), led us to consider this quantity as safe and suitable for the performance of this in vivo assay.

Tumor size evolution was measured until day 22, where the comparison ended since several tumors reached the maximum size allowed for welfare (Figure 6B). Also, a Kaplan-Meier survival analysis was performed for the different treatments. Although tumor size follow-up finished earlier, survival analysis was conducted until day 43 of the experiment (Figure 6C). Final time points for each animal were individually decided under the criteria described in the Experimental Section.

The results in Figure 6B show that the injection of Pt-NPs alone did not have any measurable effect compared to the control group, confirming that the moderate cytotoxic effect observed for U-251 MG cells in vitro is not sufficient to cause an antitumoral outcome in U-251-MG-derived xenograft tumors. This phenomenon also reinforces the idea of an enhanced radiosensitive effect, rather than an additive one. On the other hand, X-ray administration at 4 Gy + 4 Gy was effective in attaining a strong tumor reduction. However, this was further improved in the presence of Pt-NPs. Indeed, the combined treatment produced a complete tumor growth arrest until the end of the measurements, whereas tumors that underwent X-ray administration, while displaying a notably reduced size, seemed to resume their growth by the 22nd day (Figure 6B). Absolute tumor volume measurements confirmed the halted tumor progression in the combined treatment group, in contrast to the X-ray treatment alone, where tumor growth resumed, and the antitumoral effect was not sustained (Figure S13A).

The survival graphic was broadly coincident with the tumor size results (Figure 6C). However, it can be noted that the X-ray and negative control groups ended the experiment with no alive mice, followed by the Pt-NPs group, where only one mouse was considered alive after 43 days. Meanwhile, three mice belonging to the group where the combined therapy was applied were still alive after finishing the assay. This outcome suggests not only that combined therapy is clearly more effective than simple irradiation, but also that this effect can be maintained in the mid-term, slowing tumor growth and improving survival prospects during, at least, one and a half months. It should also be noted that neither the applied X-ray therapy nor the local administration of Pt-NPs produced an important weight loss in mice of the irradiated groups (Figure S13B).

Interestingly, in the survival curve (Figure 6C), the Pt-NPs-only group showed a modest delay in reaching endpoint criteria compared to the untreated control, even though its mean tumor volume continued to increase and did not exhibit a sustained macroscopic growth arrest (Figure 6B; Figure S11A,S13A). Because these experiments were performed in athymic nude mice, which lack a fully competent adaptive T-cell response, we interpret this slight survival benefit as a local intratumoral effect (e.g., focal necrosis or vascular/structural disruption at

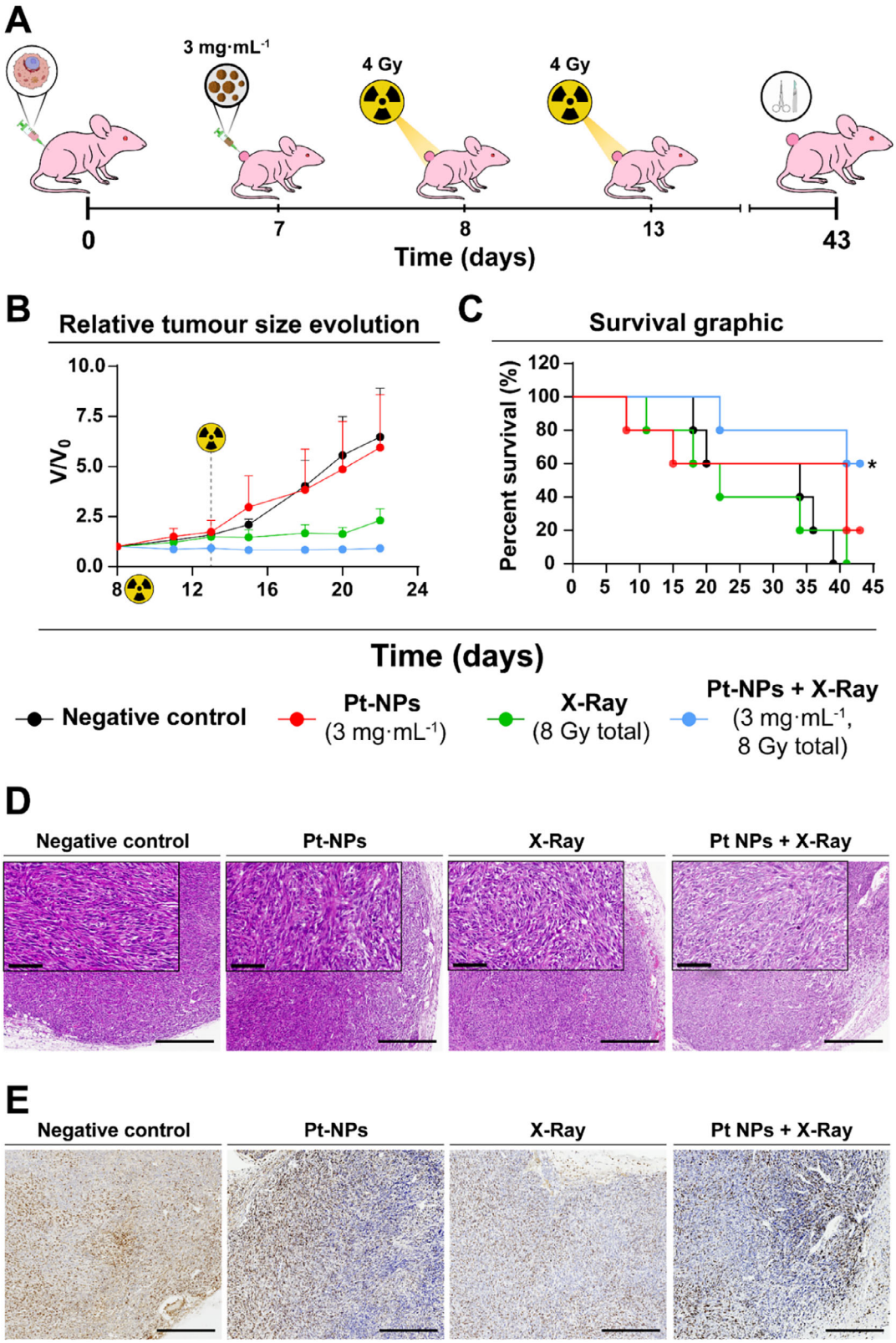

FIGURE 6 | In vivo assay (U-251 MG). (A) Schematic representation of the workflow followed for U-251 MG in vivo, from the moment U-251 MG cells were injected. (B) Evolution of the relative tumor size during the experiment, normalized by the volume measured for each individual tumor on the 8th day of the experiment (first irradiation). (C) Survival graphics of the different groups until the 43rd day. Statistical significance assessed by Long-rank (Mantel–Cox) test and Gehan–Breslow–Wilcoxon test: $*p < 0.05$. (D) Representative images of H&E staining of xenograft U-251 MG tumors of the different groups (Scale bar: 500 μm / Scale bar (insets): 100 μm). (E) Representative areas of Ki67 immunohistochemistry for xenograft tumors of the different groups (Scale bar: 500 μm). Data are shown as mean ± SEM ($n = 5$).

the injection site, or the already discussed delayed toxicity of Pt-NPs in this cell line) rather than as a systemic immune-mediated tumor rejection. In contrast, the combined Pt-NPs + X-ray treatment both limited tumor expansion and prolonged survival, indicating a more durable potentiation of RT rather than a purely local injection effect.

Hematoxylin and eosin (H&E) staining was employed to evaluate the morphological effects induced by the various treatments on the xenograft tumors derived from U-251 MG cells at the end of the experiment. In the control group, the tumors exhibited a dense and compact architecture, solid with high cellularity, and well-arranged spindle cells. The nuclei of these cells are spindle shaped, hyperchromatic, and the cytoplasm is eosinophilic (Figure 6D). This structure was maintained along all the tumoral mass, accompanied by necrotic and fibrotic zones as well as immune cell infiltration, predominantly in the central part of the tumor (Figure S14A). Pt-NPs treatment lowered cell density and produced signs of cellular damage in localized areas, yet a high organization of the cells was still perceived (Figure 6D). The tumor scanning showed notable heterogeneity, with highly organized structures, but also fibrotic and damaged areas, mainly in the tumoral core, likely due to the tumoral growth since multiple blood vessels in the lower part of the tumor scan were spotted (Figure S14B). X-ray irradiation alone reduced cellularity more clearly, showing higher spacing between cells and an increased degree of disorganization, effects that were incremented in the tumor treated with the combined therapy (Pt-NPs + X-ray) (Figure 6D). This trend was evident in most of the peripheral regions of both tumors, yet the core of the tumor treated with X-ray alone seemed to contain more organized areas than the core of the tumor that received the combined therapy. Areas of necrotic tissue, fibrosis and immune cell infiltration are also present in both tumors, and the abundance and size of blood vessels are considerably lower in the tumor that received the combined therapy than in the tumor treated with Pt-NPs (Figure S14C, S14D).

Ki67 is a nuclear protein that can be detected in proliferating cells, and does not appear to be expressed during the DNA repair process, being a critical biomarker for assessing proliferation in clinical specimens [89, 90]. The analysis of this protein showed a high degree of staining in negative control samples, especially in the periphery, with some areas of dense staining (Figure 6E). These features and spatial patterns were observed throughout the tumor mass, with a reduction of staining in the tumor core (likely related to the typical necrotic center of rapidly growing xenografts), accompanied by several zones of intense positivity (Figure S15A). Tumors treated with Pt-NPs exhibited a heterogeneous Ki67 distribution, in concordance with the H&E study, presenting highly stained areas along with several Ki67-negative regions (Figure 6E). This irregular pattern was observed across the tumor mass and, together with the high vascularization previously noted, is consistent with an aggressive and spatially heterogeneous tumor architecture (Figure S15B). Although the Ki67 signal at the experimental endpoint may appear lower in the Pt-NPs group than in the RT-only group, this should not be overinterpreted as a more effective growth suppression: tumors treated with Pt-NPs alone remained larger and continued to increase in volume over time (Figure 6B). Their heterogeneous Ki67 pattern likely reflects the presence of necrotic, hypoxic, and mechanically stressed regions (e.g., around the intratumoral injection site) with reduced local proliferation, rather than a global arrest of tumor expansion. Treatment with X-ray alone appeared to diminish Ki67 positivity in many regions, evidencing the antitumoral effect of irradiation (Figure 6E). The whole tumor mass also displayed this reduction in Ki67 expression, although relevant areas still showed proliferative foci (Figure S15C), which is consistent with the incipient regrowth trend observed for the X-ray group between the last irradiation (day 13) and the end of tumor measurements (day 22) (Figure 6B). Finally, the combined treatment (Pt-NPs + X-ray) resulted in an extensive area of Ki67-negative staining compared to all other conditions (Figure 6E). In the whole-tumor scan, although some localized Ki67-positive regions remained, most of the mass displayed weak or absent Ki67 staining (Figure S15D), and this is consistent with a persistent suppression of tumor expansion and the absence of late regrowth in that group (Figure 6B). Taken together, these findings indicate that the combination of Pt-NPs with X-ray limits the ability of the tumor to re-enter proliferation after irradiation, confirming a radiation-potentiating effect rather than a purely additive intrinsic toxicity.

2.5.2 | Intratumoral Treatment in the HeLa Xenograft Model

To compare the antitumoral effect across tumors of different origin, a parallel in vivo study was additionally conducted using a HeLa cell-derived xenograft model (Figure 7). The experimental workflow was maintained as closely as possible to the U-251 MG in vivo assay, with the first X-ray dose administered 24 h after Pt-NPs injection and a second dose delivered 5–6 days later (Figure 7A). Some minor variations in timing were necessary to adjust to the differing growth kinetics of the two tumor models. These data support coordinating irradiation with the window of maximal intratumoral Pt-NPs accumulation, rather than assuming simple size scaling, echoing the PET-based pharmacokinetics reported by Yang et al. [42]

After the subcutaneous inoculation of HeLa cells, tumors were allowed to grow until day 11, when mice received a single intratumoral injection of Pt-NPs (100 µL, 3 $mg \cdot mL^{-1}$ in PBS). X-ray irradiation was subsequently administered on days 12 and 18, delivering 4 Gy per session, and mice were monitored until day 25 (end of experiment).

The relative tumor growth evolution, normalized to day 13 (first measurement after performing the first irradiation), is shown in Figure 7B. It can be observed that, as in the case of the U-251 MG xenograft, the negative control and the Pt-NPs groups display roughly the same behavior, with a continuous progression in tumor size throughout the experiment. Also, the irradiation-only group was again effective in producing a marked reduction of tumor growth, even though continuous growth could be observed throughout the experiment. Finally, the combined Pt-NPs + RT treatment produced the best results, virtually stopping tumor growth after day 13. It can also be observed that, by the end of the experiment, the combined treatment group exhibited a statistically significant reduction in tumor size compared to the X-ray-only group, indicating enhanced antitumor efficacy mediated

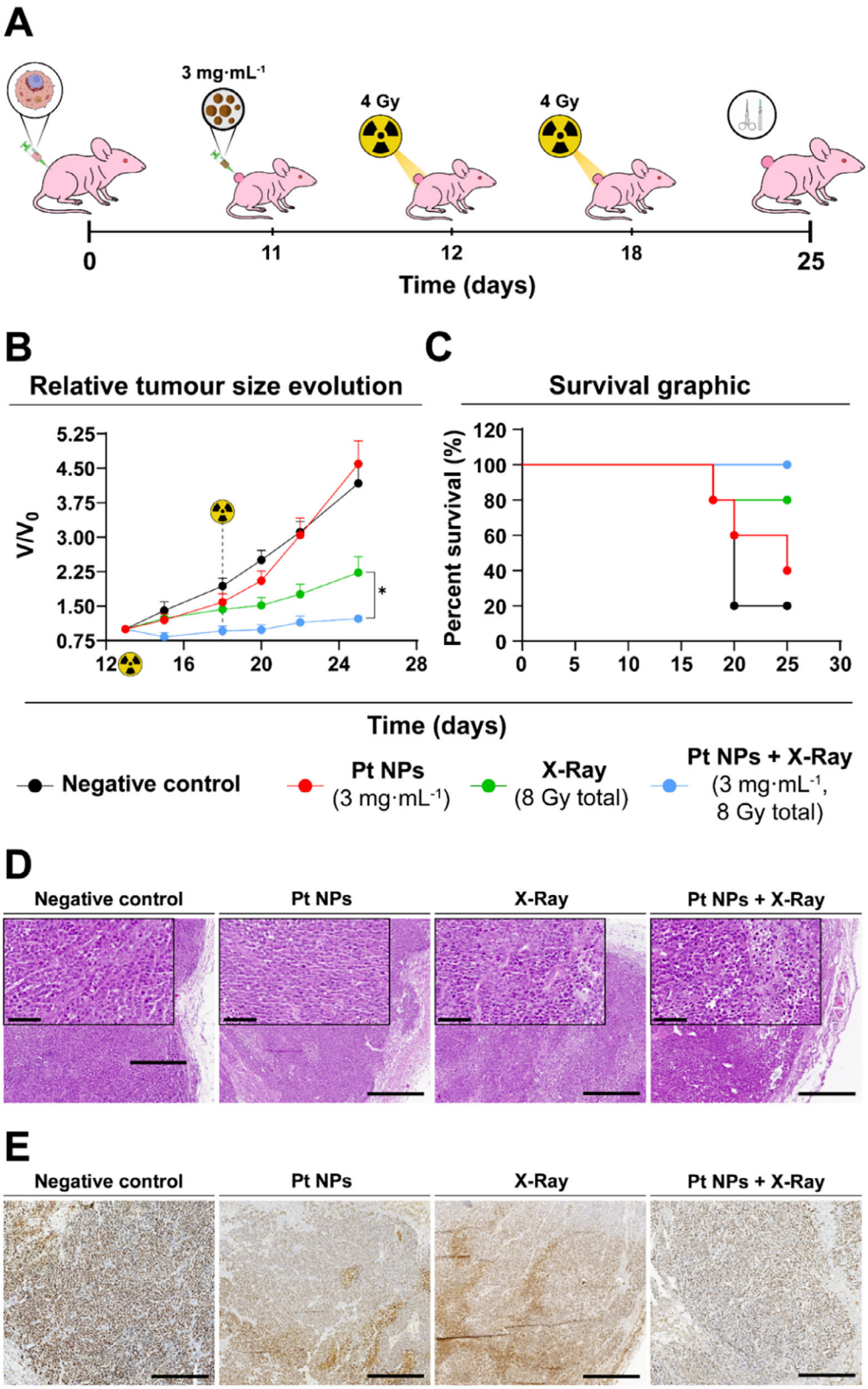

FIGURE 7 | In vivo assay (HeLa). (A) Schematic representation of the workflow followed for HeLa in vivo, from the moment the tumor cells were injected. On day 11, Pt-NPs were intratumorally injected, followed by irradiation on days 12 and 18. (B) Evolution of the relative tumor size during the experiment, normalized by the measurement of each individual tumor on the 13th day of the experiment (first performed measurement right after the first irradiation). (C) Survival graphics of the different groups until the end of the experiment (25th day). (D) Representative images of H&E staining of xenograft HeLa tumors of the different groups (Scale bar: 500 μm / Scale bar (insets): 100 μm). (E) Representative areas of Ki67 immunohistochemistry for HeLa xenograft tumors of the different groups (Scale bar: 500 μm). Data are shown as mean ± SEM ($n = 5$). Statistical significance assessed by t-test applying Welch's correction when necessary: $^*p < 0.05$.

by the addition of Pt-NPs (Figure 7B). The same trends were also observed by absolute tumor volume measurements (Figure S16A).

Also, as in the U-251 MG xenograft (although in this case the duration was shortened to 25 days), the combined treatment group yielded superior survival outcomes, with no mice reaching the predefined endpoints, although the results observed in the X-ray-only group were close (only one mice dead by day 17, Figure 7C), while 80% mortality (four mice) was observed in the control group. Irradiated groups experienced transient, mild weight loss following the first treatment, which was recovered in subsequent days and did not compromise mice welfare (Figure S16B). Lastly, the enhanced antitumor effect could also be visually corroborated by ex vivo tumor images at the final point (Figure S16C).

While intratumoral delivery was selected to maximize local concentration and demonstrate proof-of-concept radiosensitization, image-guided IT approaches are clinically established beyond superficial tumors [28]. Prospective studies will evaluate intravenous administration, pharmacokinetics, and efficacy under MV fractionations to support translatability, noting the typically low median tumor uptake after IV dosing (<1–2% ID) and the need for surface engineering and dosing optimization [91].

In general, H&E staining showed a tumor of polyhedral cells with an epithelioid appearance, large and pleomorphic. They have rounded to ovoid nuclei, with fine granular chromatin, slightly condensed toward the nuclear envelope, also presenting one or more nucleoli. The cytoplasm is moderate and eosinophilic. The cells are arranged in solid sheets. There is necrosis in all four tissues, appearing to be less present in the negative control sample, which revealed a highly organized structure, elevated cellularity and preserved architecture (Figure 7D). The full scanning of the tumor reveals this pattern in the majority of the peripheral tumoral area, also spotting certain necrotic zones with immune cell infiltration in the tumoral core (Figure S17A). Tumors treated with Pt-NPs showed a high cellular organization and density, along with the presence of necrotic spots and immune cells (Figure 7D). Similarly to the corresponding group of the U-251 MG in vivo assay, the presence of tumoral vessels across the tumor is noteworthy, also presenting areas of fibrosis, likely indicating a complex and proliferative tumoral environment (Figure S17B). The application of RT alone reveals higher tissue damage, evidencing large fibrotic areas in the tumoral periphery, which infiltrate into the more organized areas (Figure 7D). This pattern is preserved along the tumoral mass, revealing spots with lower cellular density, disorganization, necrosis and immune cell infiltration, not only restrained to the characteristic necrotic tumoral core. Still, several zones with a high organization degree can be spotted (Figure S17C). Finally, the combined Pt-NPs + X-ray group exhibited extensive tissue damage, low cell density and a higher degree of cellular disorganization (Figure 7D). Complete scanning of the tumor confirmed these features, also showing more fibrosis than necrosis along the tumoral mass, as well as barely detectable highly organized zones (Figure S17D).

Regarding the Ki67 IHQ analysis, the untreated tumors exhibited a marked staining for this protein, indicating a high proliferative activity (Figure 7E). The complete scanning of the tumor confirmed this pattern, displaying a positive staining in most of the tumoral area, markedly on the periphery, also showing spots with intense staining (Figure S18A). Tumors treated with Pt-NPs, as ascertained in the H&E staining, showed a high heterogeneity for Ki67 IHQ, exhibiting areas with negatives staining along with zones displaying an intense expression of this protein (Figure 7E). The positive areas are spread over the tumoral mass, surrounded by zones exhibiting negative staining, as well as some areas with marked staining (Figure S18B). X-ray treatment did not seem to notably affect the Ki67 expression, yet some negatively stained zones can be appreciated (Figure 7E). Indeed, the study of the whole sample revealed a high section of the tumoral mass positively stained for Ki67, whereas only localized zones demonstrated a negative Ki67-associated activity (Figure S18C). On the other hand, tumors treated with combined therapy exhibited a more homogeneous staining for Ki67. Although complete negativity for this protein was not observed, the intensity and abundance of the positive cells were lower than those observed for the rest of the treatments (Figure 7E). The complete scanning of the sample ascertained this pattern, showing a more homogeneous staining along the tumoral mass, and presenting a considerably lower positivity than the rest of the sample, also highlighting the lack of highly stained areas (Figure S18D).

2.5.3 | Intravenous Treatment in the HeLa Xenograft Model and Biosafety Evaluation

While intratumoral administration provides a controlled proof-of-concept for radiosensitization, systemic delivery represents a more clinically realistic scenario. Therefore, an additional in vivo experiment was performed where we evaluated whether intravenously injected Pt-NPs could still enhance RT efficacy under conditions where nanoparticle biodistribution, clearance, and tumor accumulation constitute limiting factors (Figure 8).

Tumor-bearing mice received two intravenous doses of Pt-NPs on days 6 and 7 (200 µL of Pt-NPs in PBS each dose, for a total Pt amount of 4.24 µg), followed by X-ray irradiation (Figure 8A). Tumor growth curves revealed that Pt-NPs alone did not significantly alter tumor progression compared with untreated controls, confirming that nanoparticles do not exert a relevant standalone antitumor effect under systemic administration (Figure 8B). Irradiation alone induced a moderate delay in tumor growth, whereas the combination of Pt-NPs plus irradiation produced a markedly stronger suppression of tumor expansion, yielding significantly smaller tumors at late time points. Similar effects were observed in the evaluation of absolute tumor size evolution during the experiment (Figure S19A).

Kaplan–Meier survival analysis showed a consistent trend (Figure 8C). Animals receiving the combined treatment exhibited the longest survival, followed by irradiation alone, whereas Pt-NPs alone behaved similarly to control animals. This demonstrates that the radiosensitizing effect observed after intratumoral administration is preserved after systemic delivery. Besides, no significant evidence of weight loss was observed during the experiment (Figure S19B).

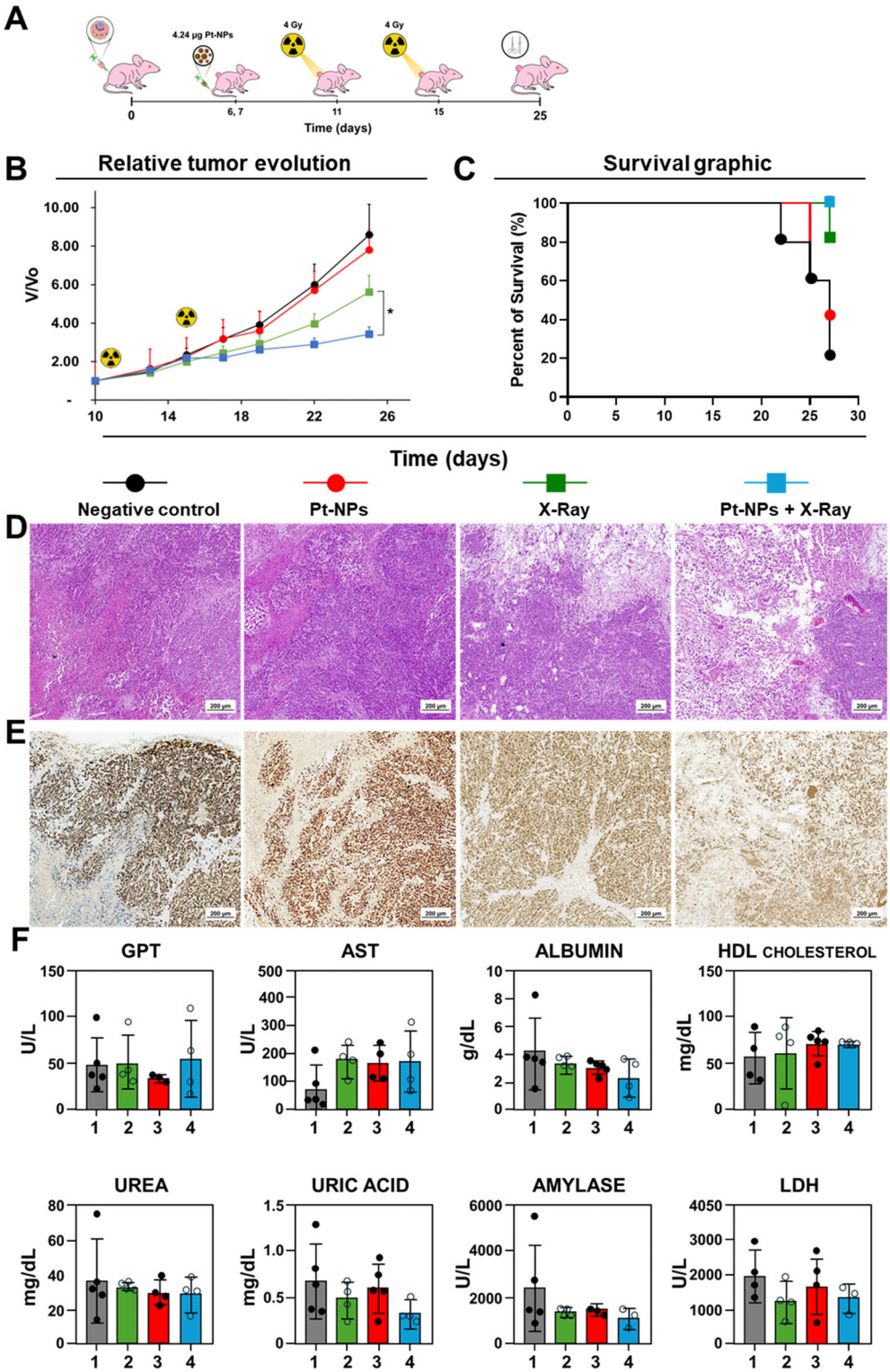

FIGURE 8 | Systemically administered ultrasmall Pt-NPs act as radiosensitizers in vivo. (A) Schematic representation of the workflow followed for HeLa in vivo, from the moment the tumor cells were injected. On days 6/7 two 200 µL containing 2.12 µg of Pt-NPs (total 4.24 µg/) were intravenously injected, followed by irradiation on days 11 and 15. (B) Evolution of the relative tumor size during the experiment, normalized by the measurement of each individual tumor on the 10th day of the experiment (first performed measurement after the first irradiation). Data are shown as mean ± SEM ($n = 5$). Statistical significance assessed by t-test applying Welch's correction when necessary: $^*p < 0.05$. (C) Survival graphics of the different groups until the end of the experiment. (D) Representative images of H&E staining of xenograft HeLa tumors of the different groups (Scale bar: 200 µm). (E) Representative areas of Ki67 immunohistochemistry for HeLa xenograft tumors of the different groups (Scale bar: 200 µm). (F) Serum biomarkers were grouped according to physiological system: hepatic (GPT/ALT, AST, albumin), renal (urea, uric acid), pancreatic (amylase), metabolic/lipid (HDL), and cytotoxicity/tissue damage (LDH). 1. Data are shown as mean ± SD (n = 3–5 per group). No statistically significant differences versus control were detected (one-way ANOVA).

Histological evaluation of tumor sections supported these macroscopic findings. Hematoxylin-eosin staining revealed extensive structural disruption, reduced cellular density, and enlarged necrotic areas in tumors treated with Pt-NPs plus irradiation compared with treatment alone (Figure 8D). Consistently, Ki67 immunohistochemistry showed a strong reduction in proliferative tumor cells in the combined treatment group, indicating suppression of tumor repopulation capacity after irradiation (Figure 8E).

To evaluate systemic safety, major organs were analyzed histologically, and serum biochemical parameters were quantified at the experimental endpoint. H&E staining of liver and kidney tissues showed preserved architecture, without necrosis, inflammatory infiltrates, or degenerative lesions in any treatment group (Figure S19C,D). Likewise, serum biomarkers associated with hepatic function (AST, GPT, albumin), renal function (urea, uric acid), tissue injury (LDH), lipid metabolism (HDL cholesterol), and pancreatic activity (amylase) remained comparable across all experimental groups, with no consistent treatment-dependent alterations (Figure 8F).

Taken together, these results demonstrate that ultrasmall Pt-NPs retain their radiosensitizing capability after intravenous administration while maintaining a favorable systemic safety profile, supporting their translational potential as RT enhancers.

In summary, the in vivo experiments corroborated the good prospects detected in vitro, with the combined treatment markedly reducing tumor growth and improving survival in both HeLa and U-251 MG xenograft models under the experimental conditions tested. RT alone achieved substantial antitumor effects at high radiation doses, but in both models, the addition of Pt-NPs amplified the radio-therapeutic outcome without apparently inducing additional toxicity. Overall, the in vivo outcome is consistent with the in vitro radiosensitization signature observed in HeLa cells. Although HeLa cells internalized less platinum than U-251 MG (Figure 4A), incubation with Pt-NPs followed by X-ray irradiation produced a significant increase in the radiation response in HeLa, quantified as a dose-modifying ratio at 50% viability (DMR_{50}(viability) > 1 after baseline correction), and the slopes of the dose-response curves for 0 $\mu g \cdot mL^{-1}$ versus 100 $\mu g \cdot mL^{-1}$ conditions were significantly different in this cell line (Figure S8). In U-251 MG, Pt-NPs also reduced viable cell number 7 days after irradiation, although part of that reduction reflects a modest delayed cytostatic/cytotoxic effect of Pt-NPs alone after prolonged exposure, rather than a pure change in the radiation dose-response slope.

Clonogenic survival is the historical gold standard to assess in vitro radiation response [92]; however, the primary endpoint in this work was different: we quantified viable adherent cell number 7 days post-irradiation, which integrates proliferative arrest and cell death across multiple doublings. We complemented this with mechanistic markers of persistent DNA damage (γH2AX and 53BP1 nuclear foci), which were more strongly induced by Pt-NPs + X-ray than by X-ray alone, particularly in HeLa cells. Further, the results of in vivo tumor growth control and survival strongly support the efficacy of the combined treatment. Together, these data confirm that Pt-NPs act as radiation enhancers under our preclinical conditions. As an additional consideration, tumors in the in vivo studies were harvested at endpoint, several days after the last irradiation, whereas γH2AX/53BP1 are transient DDR markers that peak within minutes-hours and then decline; therefore, late tumor IHC can under-represent radiosensitization. In this work, we quantified γH2AX/53BP1 at 1–2 h in vitro, showing increased DDR signaling with Pt-NPs + X-rays, and observed improved in vivo tumor control at the same radiation dose, providing concordant evidence across endpoints.

These biological findings should also be interpreted in the context of dose. In our preclinical model, the 2 × 4 Gy delivered at 185 kVp corresponds to a clinical equivalent dose (EQD2) of approximately 10–15 Gy, i.e. the low end of what is typically prescribed in the clinic. For example, definitive RT for glioblastoma is ∼60 Gy EQD2 in 2-Gy fractions, and common palliative regimens such as 20 Gy in 5 fractions correspond to ∼23 Gy EQD2 [93, 94]. The fact that Pt-NPs + X-ray therapy prevented late tumor regrowth and suppressed proliferative recovery under such modest biological dose, while X-ray therapy alone was much less efficient, is consistent with a true radiation-enhancing effect rather than a purely additive intrinsic toxicity. Further evaluation of these Pt-NPs under clinically relevant megavoltage irradiation schemes would be needed to confirm their potential.

Overall, the concordance between mechanistic assays, two tumor models, and two administration routes supports the robustness of the radiosensitizing effect observed for these ultrasmall Pt-NPs. While subcutaneous xenograft systems do not fully reproduce the complexity of native TMEs and, in particular for the glioblastoma-derived model, they do not replicate blood–brain barrier constraints or orthotopic tumor architecture, they remain well-established preclinical platforms that enable controlled comparisons between treatment conditions. Importantly, consistent therapeutic enhancement after both intratumoral and intravenous administration indicates that the observed effect is not restricted to a single delivery scenario.

3 | Conclusions

Ultrasmall (2–3 nm core) Pt-NPs exhibited radiosensitizing activity under preclinical kV X-ray irradiation, improving the antitumor effect of irradiation both in vitro and in vivo. The Pt-NPs alone displayed overall low toxicity across multiple cell lines up to 72 h, and were also well tolerated in vivo under the tested conditions, although a modest delayed cytostatic/cytotoxic effect was detected in vitro for U-251 MG after 8 days. Enhancement of RT efficiency in vitro was evidenced by: (i) a reduction in viable adherent cell number 7 days after irradiation that could not be explained by irradiation alone; (ii) a significant leftward shift in the radiation response, quantified as a dose-modifying ratio at 50% viability (DMR_{50}(viability) > 1) and a significant change in the dose-response slope in HeLa cells after correcting for baseline Pt-NPs effects; and (iii) an early and sustained increase in DNA damage signaling (γH2AX and 53BP1 nuclear foci) when Pt-NPs were combined with X-rays, particularly in HeLa.

Intratumoral administration of Pt-NPs (3 $mg \cdot mL^{-1}$) followed by two 4 Gy fractions of X-ray irradiation (total 8 Gy) produced durable suppression of tumor progression and improved survival

in both U-251 MG- and HeLa-derived xenograft models, whereas neither Pt-NPs alone nor irradiation alone could reach the same results. Comparable qualitative trends were also observed after intravenous administration, indicating that the radiosensitizing effect is not restricted to local administration and can also be achieved via systemic delivery. Based on our kV to MV biological equivalence analysis, this 2 × 4 Gy schedule corresponds to an EQD2 of ~10–15 Gy, i.e., at the low end of clinical dosing, supporting that the effect observed for the combination is not merely additive cytotoxicity at an extreme radiation dose.

Overall, these results show the potential of ultrasmall Pt-NPs as radiation enhancers for RT in preclinical models. However, we acknowledge that clonogenic survival assays under clinical MV photon energies and systemic biodistribution studies to ascertain the conditions under which a sufficient amount of Pt-NPs can be delivered to the tumor, will be required in order to foster translatability and to benchmark against existing radiosensitizing agents.

4 | Experimental Section

4.1 | Synthesis of Pt-NPs

Synthesis of Pt-PVP-2 nm (referred to in the main text as Pt-NPs) was performed using 10 000-MW PVP (Sigma Aldrich) as a stabilizer. Briefly, 100 mg of PVP were resuspended in 50 mL of dH_2O using a 250 mL 3-neck round-bottom flask. Then, 255 µL of chloroplatinic acid solution (Sigma Aldrich) (H_2PtCl_6 / MW: 409.81 g/mol / 8% w/v in H_2O) and 22.5 mL of 96% EtOH were added to the mixture, and the suspension was subsequently heated to 85°C overnight [19]. In this mixed H_2O/EtOH medium, ethanol acts both as a cosolvent and as an in situ reducing agent, promoting Pt^{4+} to Pt^0 formation, while PVP (MW 10 000) coordinates and caps the nascent Pt nuclei, preventing ripening and aggregation. PVP (10 kDa) was first dissolved in deionized water; ethanol was then added together with H_2PtCl_6 (water/ethanol mixture). Under heating (85°C), ethanol serves as the reductant, while PVP caps Pt surfaces. The PVP:Pt mass ratio in the reaction mixture was approximately 5:1 (w/w). The following day, unreacted precursors were removed after two centrifugation cycles with Amicon Ultra Centrifugal Filter (10 kDa MW CO, Merck Millipore), using 20 mL of dH_2O for the washings. The centrifugations were performed at 2080 g for 50 min at room temperature (RT). The obtained pellet was resuspended in dH_2O and stored at RT. Platinum concentration was measured through elemental analysis (MP-AES), and all concentration/dose values in the text refer to elemental platinum concentration, unless otherwise indicated. All syntheses were independently reproduced at least three times, yielding comparable nanoparticle size distributions and catalytic activity profiles, confirming batch-to-batch reproducibility.

4.2 | Characterization of Pt-NPs

Transmission electron microscopy (TEM) analysis was carried out using a FEI TECNAI T20 instrument (Tecnai, Eindhoven, The Netherlands) operated at an accelerating voltage of 200 keV. For TEM imaging, a small volume of Pt-NPs dispersion was deposited onto a holey carbon-coated copper grid and allowed to dry. Because ultrasmall metallic nanoparticles fall near or below the reliable detection limits of light-scattering-based techniques, TEM core measurements were used as the primary size descriptor throughout this study. Quantitative analysis of platinum content for the determination of Pt-NPs concentration in the samples was conducted by inductively coupled plasma mass spectrometry (ICP-MS) using a 4100 MP-AES spectrometer (Agilent Technologies, USA). Particle size distribution was evaluated by processing TEM images with ImageJ software. Structural characterization was performed using X-ray diffraction on a Malvern PANalytical Empyrean diffractometer configured in the Bragg–Brentano geometry, employing Cu Kα radiation and a PIXcel1D detector. Surface chemical composition was examined by X-ray photoelectron spectroscopy (XPS) using an Axis Ultra DLD spectrometer (Kratos Analytical) equipped with a monochromatic Al Kα X-ray source (1486.6 eV), operated at 12 kV and 10 mA. Spectra were recorded with a step energy of 20 eV, and binding energies were calibrated against the C 1s peak at 284.3 eV. Data analysis and peak fitting were conducted using CasaXPS software, employing a combination of Lorentzian and Gaussian line shapes after applying Shirley background subtraction.

4.3 | Catalase-Mimicking Activity for Molecular Oxygen Production

The ability of Pt-NPs to mimic catalase activity by generating oxygen from H_2O_2 was assessed by monitoring the generation of dissolved molecular oxygen (O_2) with the help of an oximeter. For these experiments, 1 mL of a Pt-NPs suspension at a concentration of 0.05 mg·mL^{-1} was introduced into a 2 mL reaction vial. The catalytic performance was evaluated with a first addition of 2 mL of H_2O_2 (1 mM), followed by subsequent additions of 0.05 mL of H_2O_2 (20 mM) to corroborate the sustained catalytic activity of Pt-NPs for O_2 production. Catalytic measurements were performed in cell-free buffer systems and therefore represent intrinsic nanozyme activity rather than intracellular measurements.

4.4 | Cell Lines

HeLa and U-251 MG cell lines were purchased from Cancer Research UK Cell Services. Besides, hpMSCs were purchased from Cellular Engineering Technologies Inc. All cell lines were cultured in Dulbecco's Modified Eagle's Medium (DMEM) with 4.5 g/L of glucose, supplemented with 1% Penicillin-Streptomycin-Amphotericin (PSA), 1% L-Glutamine and 10% Fetal Bovine Serum (FBS). Culture medium for hpMSCs was additionally supplemented with Recombinant Human FGF-basic (154 a.a.) at 5 µg·mL^{-1}. Cells were maintained in an incubator at 37°C and 5% CO_2.

4.5 | Cytotoxicity Assay

To study the impact of Pt-NPs on cell viability, cells were plated in 96-well plates, at a density of 3×10^3 cells per well for U-251 MG and HeLa, and 4×10^3 cells per well for hpMSCs, due to their slower growth. Cells were allowed to attach for 24 h, and subsequently, serial concentrations of Pt-NPs (ranging from 3.1 to

100 μg·mL^{-1}) were dispersed in DMEM and added to the cultures. As a control, the same volume was replaced with fresh media. Relative cell viability was measured 24, 48, and 72 h after treatment in a plate reader, using Blue Cell Viability Assay Kit (KA1605, Abnova, Taiwan), as per the manufacturer's instructions. The ratio of fluorescent values of different conditions, compared to control condition values (i.e., no treatment condition), led to the relative viability measurement for each condition. Excitation and emission wavelengths used were 528 and 590 nm, respectively.

4.6 | Pt-NPs Quantification by MP-AES

The cumulative internalization of Pt-NPs at different times was evaluated in a quantitative manner using MP-AES. Elemental quantification by MP-AES was considered the primary quantitative method for uptake determination, while microscopy techniques were used as qualitative localization tools. Briefly, 2 × 10^5 cells per well were plated in a 6 well-plate, and cells were allowed to attach for 24 h. Then, a solution of Pt-NPs in DMEM at 100 μg·mL^{-1} was added to the cells. For control conditions, an equivalent volume was replaced with fresh media. Cells were detached with a solution of 0.25% Trypsin in PBS and counted in a Neubauer chamber 24, 48, and 72 h after treatment. Subsequently, cells were centrifuged at 6700 g for 5 min, and the pellet was digested with Aqua Regia overnight, followed by a 1:5 dilution in distilled water. Then, intracellular platinum mass was quantified by Microwave Plasma Atomic Emission Spectroscopy (Agilent 4100 MP-AES).

4.7 | Internalization Assay by Confocal Microscopy

Internalization of Pt-NPs inside the cells was observed by confocal microscopy. Cells were seeded at a density of 2 × 10^4 cells in a 24-well plate, each well containing a Ø 12 mm round coverslip at the bottom. Cells were allowed to attach to the coverslip overnight, and subsequently, Pt-NPs in DMEM at 100 μg·mL^{-1} were added. Cells were washed three times with PBS 24 h after the treatment to remove non-internalized NPs, followed by fixation with 4% paraformaldehyde (PFA, Alfa Aesar) in PBS for 30 min, and three additional PBS washes. After fixation, cells were permeabilized and blocked in a 0.1% saponin-1% BSA solution in PBS (w/v). Subsequently, samples were incubated for 1 h with Phalloidin-Alexa Fluor 488 (Invitrogen) in 0.1% saponin-1% BSA solution (dilution 1:200), to stain actin fibers. Samples were then washed with 1% BSA in PBS (w/v) and with dH_2O, followed by the addition of mounting media, which was Fluoromount-G + DAPI (ANAME) for nuclei staining. Due to their metallic composition, aggregates of NPs could be observed thanks to the reflection of the incident light, and by high contrast captured with the T-PMT. These observations were performed in a ZEISS LSM 880 Confocal Microscope, using a Plan-Apochromat 63x/1.4 Oil DIC M27 objective. Due to the ultrasmall size of individual nanoparticles, only aggregated or clustered Pt-NPs can be detected by reflection-based confocal microscopy. Confocal imaging was therefore used as a method to observe aggregates and not as a quantitative internalization measurement.

4.8 | Sensitization to RT in Tumoral Cell Lines

For this experiment, 1.5 × 10^3 cells/well were seeded in 24-well plates, then allowed to attach to the wells for 24 h. Then, cells were treated with a 100 μg·mL^{-1} Pt-NPs solution in DMEM for the next 24 h (for control cells, medium was just replaced with fresh medium). After this period, cells were washed with PBS to remove the excess of noninternalized Pt-NPs, and then irradiated at different intensities (0, 1, 2, and 4 Gy). The irradiation was carried out utilizing a *MultiRad Faxitron 225* unit, a cabinet X-ray system for use as an irradiation device, placing the cell plates on the stage of the cabinet and setting up the X-ray dose of interest on the equipment. X-ray treatment was applied at preclinical energy values (185 kVp, 10 mA). Once the treatment was applied, cells were maintained in culture for 7 days from the time of irradiation (total duration of experiment: 10 days), renewing the culture medium every other day. Once the endpoint was reached, cells were detached with trypsin (0.25%) and then counted, and this workflow was performed for each condition. In this way, calculating the ratio of each condition (compared to the corresponding control conditions), a relative cell viability study could be established, thus allowing the assessment of the potential sensitization to X-rays mediated by Pt-NPs.

4.9 | γH2AX Foci Quantification

Cells were seeded at a density of 7.5 × 10^3 cells/well in several μ-slide 18-well, each well having a surface modification of #1.5 polymer coverslip. Cells were allowed to attach to the bottom overnight, and subsequently, Pt-NPs in DMEM at 100 μg·mL^{-1} were added. Then, 24 h after the treatment, cells were washed with PBS to remove noninternalized Pt-NPs, and subsequently irradiated at 4 Gy. After the corresponding time for each condition (1 or 2 h), they were washed three times with PBS, followed by fixation with 4% PFA in PBS for 10 min, and three subsequent PBS washes. After fixation, cells were permeabilized and blocked in a 0.5% Triton X-100 (v/v), 5% BSA (w/v) solution in PBS for 1 h. Subsequently, cells were washed with washing buffer (0.5% Triton X-100 (v/v), 1% BSA (w/v) solution in PBS), then incubated with primary antibody α-phospho-histone H2A.X Ser139 (9718S (20E3), Rabbit mAb #9718, Cell Signaling Technology) diluted in washing buffer overnight (dilution 1:200). The next day, samples were washed with washing buffer and then incubated with Alexa Fluor 488 Goat Anti-Rabbit IgG (Invitrogen) for 1 h in darkness, at a 1:200 dilution. Cells were then stained with Hoechst 33342 trihydrochloride trihydrate (Invitrogen) diluted 1:5000 in PBS for 10 min, rinsed in dH_2O and incubated at 4°C in PBS until the moment of sample visualization. Samples were visualized in a ZEISS LSM 880 Confocal Microscope, using a Plan-Apochromat 40X/1.3 Oil DIC UV-IR M27 objective. To quantify the effects of γH2AX, *foci* were counted using a macroinstruction in ImageJ software. For a particular image, raw data were exported from the czi file, then the nucleus area was selected in the Hoechst channel in ImageJ, supported by the nucleus silhouette. Then, this selection was applied to the Alexa Fluor 488 channel and, in the delimited areas corresponding to each nucleus, spotted points were automatically counted. Confocal settings and staining conditions were optimized to minimize background; γH2AX/53BP1 foci were

quantified with a pre-specified pipeline ("parameters in Equation S1" and S2. For each condition, n>140 nuclei were analyzed. The complete code for this macroinstruction applied to γH2AX can be found in Equation S1.

4.10 | 53BP1 Foci Quantification

Cells were seeded in a 24-well plate, at a density of 2×10^4 cells/well, each well containing a 12 mm round coverslip. Cells were incubated for 24 h to allow their attachment to the coverslip. After that, a dissolution of Pt-NPs in DMEM at 100 $\mu g \cdot mL^{-1}$ was added for 24 h. Cells were washed and media was renewed to remove noninternalized Pt-NPs, and cells were irradiated. Then, 2 h after X-ray therapy, they were washed three times with PBS, followed by fixation with 4% PFA in PBS for 10 min, and three additional PBS washes. After fixation, coverslips were permeabilized and blocked in a 0.5% Triton X-100 (v/v) and 5% BSA (w/v) solution in PBS for 1 h. After that incubation, cells were washed with washing buffer and then incubated with the primary antibody α-53BP1 (4937S, #4937, Cell Signaling Technology) overnight at a 1:100 dilution. The next day, coverslips were rinsed with washing buffer and then incubated with Alexa Fluor 488 Goat Anti-Rabbit IgG (Invitrogen) for 1 h in darkness. Finally, cells were washed one more time with washing buffer and stained with Hoechst 33342 trihydrochloride trihydrate (Invitrogen) diluted 1:5000 in PBS for 10 min. One last rinse in dH_2O was performed, and then coverslips were mounted in slides with ProLong Glass Antifade Mountant (Invitrogen). Samples were visualized in a ZEISS LSM 880 Confocal Microscope, using a Plan-Apochromat 40X/1.3 Oil DIC UV-IR M27 objective. To quantify the effects of 53BP1, *foci* were counted using a macroinstruction in ImageJ software. For a particular image, raw data were exported from the czi file, then the nucleus area was selected in the Hoechst channel in ImageJ, supported by the nucleus silhouette. Then, this selection was applied to the Alexa Fluor 488 channel and, in the delimited areas corresponding to each nucleus, spotted points were automatically counted. The complete code for this macroinstruction applied to 53BP1 can be found in Equation S2.

4.11 | ROS Generation Analysis with H_2DFCDA

ROS generation mediated by Pt-NPs was studied using the probe 2′,7′-Dichlorodihydrofluorescein diacetate (H_2DFCDA, Thermo Fisher Scientific). This nonfluorescent compound, in the presence of oxidant species, gets oxidized to highly fluorescent 2′,7′-dichlorofluorescein (DCF), revealing the presence of intracellular ROS. Considering this, 4×10^4 cells per well (U-251 MG or HeLa) were seeded in a 24-well plate. After cell attachment (24 h), cells were treated with 100 $\mu g \cdot mL^{-1}$ of Pt-NPs for another 24 h. After that time, cells were washed with PBS to remove noninternalized Pt-NPs, then incubated with a solution of 10 μM H_2DCFDA in PBS for 30 min at 37°C. Cells were then washed again to eliminate the noninternalized probe, and subsequently irradiated at 4 Gy. Then, 30 min after the irradiation, cells were washed and incubated in a lysis buffer (Tris-HCl + NaCl + Triton X-100) for 40 min. After that time, the fluorescence of the different wells was measured in a TECAN plate reader (Ex: 484 nm/Em: 529 nm).

4.12 | Licenses and Animal Models

Animal experiments were reviewed and approved by the Research Ethics and Animal Welfare Committee of *Instituto de Salud Carlos III*, Madrid (PROEX 235.0/22) and performed according to the Spanish Policy for Animal Protection RD53/2013 and the European Union Directive 2010/63 regarding the protection of animals destined for experimental and other scientific purposes. For these assays, 6 to 10-week female Hsd:Athymic Nude-Fox1nu mice acquired from Envigo were used. At the moment of their arrival, animals remained under quarantine for 1 week, and they were fed ad libitum during all the experiments, keeping a 12 h light-dark cycle under sterile conditions. When the experiments were finished, the mice were sacrificed using a CO_2 chamber.

4.13 | Protocol of Mice Irradiation

Irradiation of mice was performed with the same *Multirad Faxitron 225* X-ray irradiator that was used for in vitro assays. To perform X-ray administration, mice were anesthetized with a mixture of ketamine (75 mg/kg) and medetomidine (0.5 mg/kg) injected intraperitoneally. When mice were asleep, they were transported in a closed box to the irradiator. Before applying X-ray treatment, a hydrating lotion was applied to mice's eyes to avoid drying during the anesthesia effect. Mice were then disposed inside the irradiation chamber, covered with plumbed paper in a way that only the xenograft tumor was exposed to the irradiation source, thus protecting the rest of the body.

X-ray treatment consisted of two fractions of 4 Gy delivered with a 185 kVp cabinet X-ray unit (10 mA), separated by 5 days. To aid translation and assuming the modestly higher relative biological effectiveness (RBE) of kV versus clinical MV photons (RBE ≈ 1.1–1.2), each 4 Gy kV fraction is approximately equivalent to 4.4–4.8 Gy with 6–15 MV beams; thus, our 2 × 4 Gy kV course approximates 2 × 4.4–4.8 Gy MV. We also report the regimen as EQD2 (equivalent dose in 2-Gy fractions), the linear-quadratic conversion that expresses any fractionation as a biologically equivalent 2-Gy schedule to facilitate comparison with clinical regimens. Full RBE assumptions and EQD2 calculations are provided in Methods S1.

When the irradiation was completed, mice were treated with the reversal agent (Atipamezole, 1.25 mg/kg), intraperitoneally administered, to allow them recover from anesthesia. Mice were then transported back to their cages and monitored until they were completely awake.

4.14 | In Vivo Antitumoral Evaluation in Xenograft Tumor Models

Two human tumor xenograft models were used: U-251 MG glioblastoma and HeLa cervical carcinoma. Tumors were established by subcutaneous injection of tumor cells into the flank of 6–10-week-old athymic female mice. U-251 MG tumors were generated using 7×10^6 cells suspended in 200 μL Matrigel:PBS (1:1 v/v), whereas HeLa tumors were induced using 2×10^6 cells in 200 μL PBS. Tumor growth was monitored periodically until

treatment initiation. Before treatment, animals were randomly assigned to four experimental groups with matched mean tumor volumes to ensure inter-group homogeneity: (i) control (no treatment, no irradiation), (ii) X-ray only, (iii) Pt-NPs only, and (iv) Pt-NPs + X-ray. Two administration routes were evaluated. Intratumoral administration (U-251MG and HeLa models) was selected to directly assess intrinsic radiosensitizing capacity independently of pharmacokinetic and delivery barriers, whereas intravenous administration (HeLa model) was used to evaluate systemic tolerance and translational feasibility.

Intratumoral administration. For the U-251 MG model, a single intratumoral injection of Pt-NPs (100 µL at 3 $mg{\cdot}mL^{-1}$concentration) was administered on day 7 after tumor inoculation (average tumor volume approximately 0.17 cm^3). For the HeLa model, the same single intratumoral injection was administered on day 11 (average tumor volume approximately 0.25 cm^3). X-ray irradiation (4 Gy per time) was applied 24 h after Pt-NPs injection and repeated 5–6 days later (days 8 and 13 for U-251 MG, and days 12 and 18 for HeLa).

Intravenous administration. For systemic delivery experiments, HeLa tumor-bearing mice received two intravenous injections of Pt-NPs in 200 µL of PBS (4.24 µg of total Pt mass) on days 6 and 7 after tumor inoculation. X-ray irradiation (4 Gy) was subsequently administered on days 11 and 15. Tumor size and body weight were recorded every other day. Relative tumor volume values were calculated with respect to the first post-irradiation measurement for each model. Survival analysis considered animals to have reached endpoint when any of the following criteria were met: death, tumor volume >1.5 cm^3, or body-weight loss ≥15% sustained for two consecutive days. Animal welfare was continuously monitored, and humane endpoints were applied in accordance with institutional ethical guidelines. Kaplan–Meier survival curves were generated using GraphPad Prism 8.0.1.

4.15 | Histological and Immunohistochemical Analysis

Extracted tumors and organs were fixed in 4% paraformaldehyde in PBS, then rinsed and stored at 4°C in 70% ethanol. Samples were dehydrated through graded ethanol solutions and embedded in paraffin using an automated tissue processor (Leica TP1020) and embedding station (Leica EG1150H). Paraffin blocks were sectioned at 3 µm thickness with a rotary microtome (Leica RM2255) and mounted on glass slides.

Hematoxylin and eosin (H&E) staining was performed at a certified histopathology core facility using standard protocols. Briefly, sections were deparaffinized in xylene, rehydrated through graded ethanol solutions, stained with Carazzi's hematoxylin followed by eosin, dehydrated, cleared, and mounted with permanent mounting medium.

For immunohistochemical detection of Ki67, sections were first deparaffinized and rehydrated as described above. Antigen retrieval was performed using a PT Link system (Dako) at 95°C for 20 min in low-pH retrieval buffer (Dako). Endogenous peroxidase activity was blocked using EnVision FLEX Peroxidase Blocking reagent, followed by incubation with ready-to-use anti-Ki67 primary antibody for 20 min. Signal detection was carried out using an ABC-based visualization system (Quimigen) with 3,3′-diaminobenzidine (DAB) as chromogen. Slides were counterstained, dehydrated, and mounted. Histological sections were examined under bright-field microscopy, and representative images were acquired at multiple magnifications.

4.16 | Statistical Analysis

Data were treated with GraphPad Prism 8.0.1 software. Results of the experiments are expressed as mean ± standard deviation (SD). Absolute and relative tumor size evolution, as well as mouse weight evolution, are expressed as mean ± standard error of the mean (SEM). Outlier detection in the experiments was performed and analyzed with the ROUT method ($Q = 1\%$). Significance analysis was carried out by performing a two-tailed unpaired *t*-test assuming a Gaussian distribution and applying Welch's correction when necessary. Statistically significant differences were expressed as: * ($p < 0.05$), ** ($p < 0.01$), *** ($p < 0.001$), and **** ($p < 0.0001$).

Author Contributions

M.E.G., J.I.G.P., P.M.D., E.C., and A.D.L.V. performed the experiments and analyzed the data. F.H.A., J.I.G.P, and J.L.H. synthetized and characterized the Pt-NPs. J.L.H., P.M.D., A.D.L.V., and J.S. designed, coordinated, and supervised the research. M.E.G., A.D.L.V., J.S. and J.I.G.P. wrote the original draft of the article. All the authors contributed to the edition and review and gave approval to the final version of the manuscript.

Acknowledgements

The authors would like to acknowledge funding from the European Research Council (ERC) through project ERC-2016-ADG 742684 (CADENCE) and the Spanish Ministry of Economy and Competitiveness through Project PID2023-148732NB-I00 and PID2021-125948OB-I00. The authors would like to thank the Scientific Services of the Instituto Aragones de Ciencias de la Salud (IACS), specifically the Microscopy and Imaging Service, and the Core Pathology Unit. Similarly, we acknowledge the scientific-technical services of Instituto de Salud Carlos III, especially the Microscopy and Imaging Service, the Histology Unit and the Animal Facilities Service. The authors also thank CIBER-BBN, an initiative funded by the VI National R&D&i Plan 2008–2011 financed by the Instituto de Salud Carlos III with the assistance of the European Regional Development Fund. The synthesis of materials has been performed by the Platform of Production of Biomaterials and Nanoparticles of the NANBIOSIS ICTS, more specifically by the Nanoparticle Synthesis Unit of the CIBER in BioEngineering, Biomaterials and Nanomedicine (CIBER-BBN). The TEM studies were conducted at the Laboratorio de Microscopias Avanzadas, Instituto de Nanociencia y Materiales de Aragon, Universidad de Zaragoza, Spain (SAI and ICTS ELECMI). Severo Ochoa funds (CEX2023-001286-S) are acknowledged by MICIU/AEI/10.13039/501100011033.

Funding

The authors would like to acknowledge funding from the ERC Advanced Grant CADENCE project number 742684 and from Spanish Government Grant PID2023-148732NB-100. A.D.L.V acknowledges the Spanish Government grant PID2021-125948OB-I00 from MCIN/AEI/10.13039/501100011033/FEDER (UE) and P.M.D funding from Instituto de Salud Carlos lll, AESI 2024 PI24CIII/00046 and Ministerio de Ciencia, Innovación y Universidades. CNS2023-145442. The authors also thank CIBER-BBN, an initiative funded by

the VI National R&D&i Plan 2008–2011 financed by the Instituto de Salud Carlos III (ISCIII) with the assistance of the European Regional Development Fund. M.E.G. and J.I.G.P. acknowledge the Aragon Regional Government for their predoctoral contracts. F.H. acknowledges the Generalitat Valenciana and the European Social Fund for an APOSTD fellowship (APOSTD/2021/196). The study was also supported by the Aragon Government via Research Group T57_23R. Severo Ochoa (CEX2023-001286-S) is acknowledged by MICIU/AEI/10.13039/501100011033.

Conflicts of Interest

The authors declare no conflicts of interest.

Data Availability Statement

The data that support the findings of this study are available in the supplementary material of this article.

References

1. "Cancer Statistics," National Cancer Institute, accessed June 5, 2025, https://www.cancer.gov/about-cancer/understanding/statistics.

2. M. Sancho-Albero, A. Martin-Pardillos, L. Lujan, V. Sebastian, J. Santamaria, and P. Martin-Duque, "Exosomes Loaded With Ultrasmall Pt Nanoparticles: A Novel Low-Toxicity Alternative to Cisplatin," *Journal of Nanobiotechnology* 20 (2022): 473.

3. Z. Fan, S. Wu, H. Deng, G. Li, L. Huang, and H. Liu, "Light-Triggered Nanozymes Remodel the Tumor Hypoxic and Immunosuppressive Microenvironment for Ferroptosis-Enhanced Antitumor Immunity," *ACS Nano* 18 (2024): 12261–12275.

4. Z. Wang, D. Wang, X. Ren, et al., "One Stone, Three Birds: Multifunctional Nanodots as "Pilot Light" for Guiding Surgery, Enhanced Radiotherapy, and Brachytherapy of Tumors," *ACS Central Science* 9 (2023): 1976–1988.

5. "The Science Behind Radiation Therapy," American Cancer Society, accessed June 16, 2025, https://www.cancer.org/content/dam/CRC/PDF/Public/6151.00.pdf.

6. "Radiation Therapy to Treat Cancer," National Cancer Institute, accessed June 16, 2025, https://www.cancer.gov/about-cancer/treatment/types/radiation-therapy.

7. Y. Zhang, X. Li, X. Ren, et al., "Nanozymes as Glucose Scavengers and Oxygenerators for Enhancing Tumor Radiotherapy," *ACS Applied Materials & Interfaces* 16 (2024): 61805–61819.

8. Z. Wang, X. Ren, Y. Li, et al., "Reactive Oxygen Species Amplifier for Apoptosis-Ferroptosis Mediated High-Efficiency Radiosensitization of Tumors," *ACS Nano* 18 (2024): 10288–10301.

9. M. Haque, M. S. Shakil, and K. M. Mahmud, "The Promise of Nanoparticles-Based Radiotherapy in Cancer Treatment," *Cancers* 15 (2023): 1892.

10. W. Liu, B. Chen, H. Zheng, et al., "Advances of Nanomedicine in Radiotherapy," *Pharmaceutics* 13 (2021): 1757.

11. P. Wardman, "Chemical Radiosensitizers for Use in Radiotherapy," *Clinical Oncology* 19 (2007): 397–417.

12. A. E. Kabakov and A. O. Yakimova, "Hypoxia-Induced Cancer Cell Responses Driving Radioresistance of Hypoxic Tumors: Approaches to Targeting and Radiosensitizing," *Cancers* 13 (2021): 1102.

13. L. Qian, Q. Li, Z. Ding, et al., "Prodrug Nanosensitizer Overcomes the Radiation Resistance of Hypoxic Tumor," *ACS Applied Materials & Interfaces* 14 (2022): 56454–56470.

14. C.-H. Lin, C.-J. Feng, Y.-C. Lai, S.-C. Tseng, C.-H. Wu, and S.-M. Hsu, "Evaluate the Effects of Kilovoltage Transmission Target X-Ray Equipment Combined With Radiosensitizers for Auger Electron Radiotherapy," *Radiation Physics and Chemistry* 215 (2024): 111320.

15. J. A. Nickoloff, L. Taylor, N. Sharma, and T. A. Kato, "Exploiting DNA Repair Pathways for Tumor Sensitization, Mitigation of Resistance, and Normal Tissue Protection in Radiotherapy," *Cancer Drug Resistance* 4 (2021): 244–263.

16. Y. Zheng and L. Sanche, "Mechanisms of Nanoscale Radiation Enhancement by Metal Nanoparticles: Role of Low Energy Electrons," *International Journal of Molecular Science* 24 (2023): 4697.

17. L. Ma, Y. Wang, X. Wang, et al., "Transition Metal Complex-Based Smart AIEgens Explored for Cancer Diagnosis and Theragnostics," *Coordination Chemistry Reviews* 473 (2022): 214822.

18. Z. Yang, S. Huang, Y. Liu, et al., "Biotin-Targeted Au(I) Radiosensitizer for Cancer Synergistic Therapy by Intervening With Redox Homeostasis and Inducing Ferroptosis," *Journal of Medicinal Chemistry* 65 (2022): 8401–8415.

19. J. F. Hainfeld, D. N. Slatkin, and H. M. Smilowitz, "The Use of Gold Nanoparticles to Enhance Radiotherapy in Mice," *Physics in Medicine and Biology* 49 (2004): N309–N315.

20. Y. Li, K. H. Yun, H. Lee, S. H. Goh, Y. G. Suh, and Y. Choi, "Porous Platinum Nanoparticles as a High-Z and Oxygen Generating Nanozyme for Enhanced Radiotherapy In Vivo," *Biomaterials* 197 (2019): 12–19.

21. E. Porcel, S. Liehn, H. Remita, et al., "Platinum Nanoparticles: A Promising Material for Future Cancer Therapy?," *Nanotechnology* 21 (2010): 085103.

22. H. Song, H. Sun, N. He, et al., "Gadolinium-Based Ultra-Small Nanoparticles Augment Radiotherapy-Induced T-Cell Response to Synergize With Checkpoint Blockade Immunotherapy," *Nanoscale* 14 (2022): 11429–11442.

23. H. Sun, H. Cai, C. Xu, et al., "AGuIX Nanoparticles Enhance Ionizing Radiation-Induced Ferroptosis on Tumor Cells by Targeting the NRF2-GPX4 Signaling Pathway," *Journal of Nanobiotechnology* 20 (2022): 449.

24. S. B. Owusu, A. Zaher, S. Ahenkorah, D. N. Pandya, T. J. Wadas, and M. S. Petronek, "Gallium Uncouples Iron Metabolism to Enhance Glioblastoma Radiosensitivity," *International Journal of Molecular Sciences* 25 (2024): 10047.

25. Y. Wang, H. Zhang, Y. Liu, M. H. Younis, W. Cai, and W. Bu, "Catalytic Radiosensitization: Insights From Materials Physicochemistry," *Materials Today* 57 (2022): 262–278.

26. P. Zhang, J. Marill, A. Darmon, N. Mohamed Anesary, B. Lu, and S. Paris, "NBTXR3 Radiotherapy-Activated Functionalized Hafnium Oxide Nanoparticles Show Efficient Antitumor Effects Across a Large Panel of Human Cancer Models," *International Journal of Nanomedicine* 16 (2021): 2761–2773.

27. S. Bonvalot, C. Le Pechoux, T. De Baere, et al., "First-in-Human Study Testing a New Radioenhancer Using Nanoparticles (NBTXR3) Activated by Radiation Therapy in Patients With Locally Advanced Soft Tissue Sarcomas," *Clinical Cancer Research* 23 (2017): 908–917.

28. S. Bonvalot, P. L. Rutkowski, J. Thariat, et al., "NBTXR3, a First-in-Class Radioenhancer Hafnium Oxide Nanoparticle, Plus Radiotherapy Versus Radiotherapy Alone in Patients With Locally Advanced Soft-Tissue Sarcoma (Act.In.Sarc): A Multicentre, Phase 2–3, Randomised, Controlled Trial," *Lancet Oncology* 20 (2019): 1148–1159.

29. "JNJ-90301900 (NBTXR3) Activated by Radiotherapy With or Without Cetuximab in LA-HNSCC," ClinicalTrials.gov, accessed August 28, 2025, https://clinicaltrials.gov/study/NCT04892173?term=NBTXR3&page=2&rank=13.

30. G. Bort, F. Lux, S. Dufort, Y. Cremillieux, C. Verry, and O. Tillement, "EPR-Mediated Tumor Targeting Using Ultrasmall-Hybrid Nanoparticles: From Animal to Human With Theranostic AGuIX Nanoparticles," *Theranostics* 10 (2020): 1319–1331.

31. "AGuIX Nanoparticles With Radiotherapy Plus Concomitant Temozolomide in the Treatment of Newly Diagnosed Glioblastoma (NANO-GBM)," ClinicalTrials.gov, accessed August 28, 2025, https://clinicaltrials.gov/study/NCT04881032?term=AGuIX%20&rank=1.

32. "Stereotactic Brain-directed Radiation With or Without Aguix Gadolinium-Based Nanoparticles in Brain Metastases," ClinicalTrials.gov, accessed August 28, 2025, https://clinicaltrials.gov/study/NCT04899908?term=AGuIX%20&rank=6.

33. S. Rottenberg, C. Disler, and P. Perego, "The Rediscovery of Platinum-Based Cancer Therapy," *Nature Reviews Cancer* 21 (2021): 37–50.

34. J. I. Garcia-Peiro, J. Bonet-Aleta, J. Santamaria, and J. L. Hueso, "Platinum Nanoplatforms: Classic Catalysts Claiming a Prominent Role in Cancer Therapy," *Chemical Society Reviews* 51 (2022): 7662–7681.

35. J. I. Garcia-Peiro, M. C. Ortega-Liebana, C. Adam, et al., "Dendritic Platinum Nanoparticles Shielded by Pt-S PEGylation as Intracellular Reactors for Bioorthogonal Uncaging Chemistry," *Angewandte Chemie* 64 (2025): 202424037.

36. J. I. Garcia-Peiro, J. Bonet-Aleta, M. L. Tamayo-Fraile, and J. L. Hueso, "Platinum-Based Nanodendrites as Glucose Oxidase-Mimicking Surrogates," *Nanoscale* 15 (2023): 14399–14408.

37. Y. Xin, J.-G. Liu, Y. Zhou, et al., "Preparation and Characterization of Pt Supported on Graphene With Enhanced Electrocatalytic Activity in Fuel Cell," *Journal of Power Sources* 196 (2011): 1012–1018.

38. J. I. Garcia-Peiro, J. Bonet-Aleta, and J. L. Hueso, "Copper-Based Nanoplatforms and Their Role in Cancer Therapy," *Coordination Chemistry Reviews* 534 (2025): 216542.

39. N. Hoshyar, G. Samantha, and H. Hongbin, "The Effect of Nanoparticle Size on In Vivo Pharmacokinetics and Cellular Interaction," *Nanomedicine* 11 (2016): 673–692.

40. E. Loscertales, R. Lopez-Mendez, J. Mateo, et al., "Impact of Gold Nanoparticle Size and Coating on Radiosensitization and Generation of Reactive Oxygen Species in Cancer Therapy," *Nanoscale Advances* 7 (2025): 1204–1214.

41. D. Cassano, A.-K. Mapanao, M. Summa, et al., "Biosafety and Biokinetics of Noble Metals: The Impact of Their Chemical Nature," *ACS Applied Bio Materials* 2 (2019): 4464–4470.

42. X. Yang, V. L. Tran, H. Remita, et al., "Pharmacokinetics Derived From PET Imaging of Inspiring Radio-Enhancer Platinum Nanoparticles," *Nanomedicine: Nanotechnology, Biology and Medicine* 46 (2022): 102603.

43. H. S. Choi, W. Liu, P. Misra, et al., "Renal Clearance of Quantum Dots," *Nature Biotechnology* 25 (2007): 1165–1170.

44. R. George, L. Fétiveau, E. Porcel, et al., "Ultra-Small Platinum-Based Coordination Nanoparticles for Radiotherapy," *Materials Advances* 4 (2023), 5314–5323.

45. E. Pagáčová, L. Štefančíková, F. Schmidt-Kaler, et al., "Challenges and Contradictions of Metal Nano-Particle Applications for Radio-Sensitivity Enhancement in Cancer Therapy," *International Journal of Molecular Sciences* 20 (2019): 588.

46. D. Salado-Leza, E. Porcel, X. Yang, et al., "Green One-Step Synthesis of Medical Nanoagents for Advanced Radiation Therapy," *Nanotechnology, Science and Applications* 13 (2020): 61–76.

47. R. Zhang, Y. Shen, X. Zhou, et al., "Hypoxia-Tropic Delivery of Nanozymes Targeting Transferrin Receptor 1 for Nasopharyngeal Carcinoma Radiotherapy Sensitization," *Nature Communications* 16 (2025): 890.

48. Y. Xin, T. Nagata, K. Kato, Y. Xu, and T. Shirai, "Role of Polyvinylpyrrolidone in the Polyol Synthesis of Platinum Nanoparticles," *Nanoscale Advances* 6 (2024): 3034–3040.

49. J. Bonet-Aleta, J. I. Garcia-Peiro, S. Irusta, and J. L. Hueso, "Gold-Platinum Nanoparticles With Core–Shell Configuration as Efficient Oxidase-Like Nanosensors for Glutathione Detection," *Nanomaterials* 12 (2022): 755.

50. Q. Ma, L. Cheng, F. Gong, et al., "Platinum Nanoworms for Imaging-Guided Combined Cancer Therapy in the Second Near-Infrared Window†," *Journal of Materials Chemistry B* 6 (2018): 5069.

51. Y. K. Hou, Z. J. Zhang, R. T. Li, et al., "Remodeling the Tumor Microenvironment With Core–Shell Nanosensitizer Featuring Dual-Modal Imaging and Multimodal Therapy for Breast Cancer," *ACS Applied Materials & Interfaces* 15 (2023): 2602–2616.

52. S. Yang, G. Han, Q. Chen, et al., "Au-Pt Nanoparticle Formulation as a Radiosensitizer for Radiotherapy With Dual Effects," *International Journal of Nanomedicine* 16 (2021): 239–248.

53. M. D. M. Encabo-Berzosa, M. Sancho-Albero, A. Crespo, et al., "The Effect of PEGylated Hollow Gold Nanoparticles on Stem Cell Migration: Potential Application in Tissue Regeneration," *Nanoscale* 9 (2017): 9848–9858.

54. K. Yaray, A. Norbakhsh, H. Rashidzadeh, et al., "Chemoradiation Therapy of 4T1 Cancer Cells With Methotrexate Conjugated Platinum Nanoparticles Under X-Ray Irradiation," *Inorganic Chemistry Communications* 150 (2023): 110457.

55. X. Yang, D. Salado-Leza, E. Porcel, et al., "A Facile One-Pot Synthesis of Versatile PEGylated Platinum Nanoflowers and Their Application in Radiation Therapy," *International Journal of Molecular Sciences* 21 (2020): 1619.

56. K. Wawrowicz, A. Majkowska-Pilip, M. Szwed, K. Żelechowska-Matysiak, E. Chajduk, and A. Bilewicz, "Oxidative Status as an Attribute for Selective Antitumor Activity of Platinum-Containing Nanoparticles Against Hepatocellular Carcinoma," *International Journal of Molecular Sciences* 23 (2022): 14773.

57. M. Hullo, R. Grall, Y. Perrot, et al., "Radiation Enhancer Effect of Platinum Nanoparticles in Breast Cancer Cell Lines: In Vitro and In Silico Analyses," *International Journal of Molecular Sciences* 22 (2021): 4436.

58. X. Liu, X. Zhang, M. Zhu, et al., "PEGylated Au@Pt Nanodendrites as Novel Theranostic Agents for Computed Tomography Imaging and Photothermal/Radiation Synergistic Therapy," *ACS Applied Materials & Interfaces* 9 (2017): 279–285.

59. W. Jiang, L. Wei, B. Chen, et al., "Platinum Prodrug Nanoparticles Inhibiting Tumor Recurrence and Metastasis by Concurrent Chemoradiotherapy," *Journal of Nanobiotechnology* 20 (2022): 129.

60. G. Liang, X. Jin, S. Zhang, and D. Xing, "RGD Peptide-Modified Fluorescent Gold Nanoclusters as Highly Efficient Tumor-Targeted Radiotherapy Sensitizers," *Biomaterials* 144 (2017): 95–104.

61. R. Benlloch, R. Castejon, S. Rosado, M. J. Coronado, P. Sanchez, and J. Romero, "In Vitro Radiosensitization by Eribulin in Human Cancer Cell Lines," *Reports of Practical Oncology and Radiotherapy* 27 (2022): 509.

62. Z. Liu, H. Tan, X. Zhang, et al., "Enhancement of Radiotherapy Efficacy by Silver Nanoparticles in Hypoxic Glioma Cells," *Artificial Cells, Nanomedicine, and Biotechnology* 46 (2018): 922.

63. C. A. Burmeister, S. F. Khan, G. Schafer, et al., "Cervical Cancer Therapies: Current Challenges and Future Perspectives," *Tumour Virus Research* 13 (2022): 200238.

64. C. Fernandes, A. Costa, and L. Osorio, "Current Standards of Care in Glioblastoma Therapy," in *Glioblastoma*, ed. S. De Vleeschouwer (Exon, 2017) 29251860.

65. *IAEA Human Health Reports No. 17* (International Atomic Energy Agency, 2022).

66. O. Senkesen, E. Tezcanli, M. U. Abacioglu, et al., "Limited Field Adaptive Radiotherapy for Glioblastoma: Changes in Target Volume and Organ at Risk Doses," *Radiation Oncology Journal* 40 (2022): 9–19.

67. A. I. S. Holm, J. B. B. Petersen, L. P. Muren, K. Seiersen, P. Borghammer, and S. Lukacova, "Functional Image-Guided Dose Escalation in Gliomas Using of State-of-the-Art Photon vs. Proton Therapy," *Acta Oncologica* 56 (2017): 826–831.

68. L. Kumar, G. Yadav, K. Raman, M. Bhushan, and M. Pal, "The Dosimetric Impact of Different Photon Beam Energy on RapidArc Radiotherapy Planning for Cervix Carcinoma," *Journal of Medical Physics* 40 (2015): 207–213.

69. A. Tyagi, S. S. Supe, Sandeep, and M. P. Singh, "A Dosimetric Analysis of 6 MV Versus 15 MV Photon Energy Plans for Intensity Modulated Radiation Therapy (IMRT) of Carcinoma of Cervix," *Reports of Practical Oncology & Radiotherapy* 15 (2010): 125–131, https://doi.org/10.1016/j.rpor.2010.08.002.

70. L. Minafra, N. Porcino, V. Bravata, et al., "Radiosensitizing Effect of Curcumin-Loaded Lipid Nanoparticles in Breast Cancer Cells," *Scientific Reports* 9 (2019): 11134.

71. L. R. H. Gerken, A. Gogos, F. H. L. Starsich, et al., "Catalytic Activity Imperative for Nanoparticle Dose Enhancement in Photon and Proton Therapy," *Nature Communications* 13 (2022): 3248.

72. L. J. Kuo and L. X. Yang, "Gamma-H2AX - A Novel Biomarker for DNA Double-Strand Breaks," *In Vivo* 22 (2008): 305–309.

73. J. Ma, Y. Zhou, P. Pan, et al., "TRABID Overexpression Enables Synthetic Lethality to PARP Inhibitor Via Prolonging 53BP1 Retention at Double-Strand Breaks," *Nature Communications* 14 (2023): 1810.

74. S. Nakada, R. M. Yonamine, and K. Matsuo, "RNF8 Regulates Assembly of RAD51 at DNA Double-Strand Breaks in the Absence of BRCA1 and 53BP1," *Cancer Research* 72 (2012): 4974–4983.

75. B. Martinez-Pastor, G. G. Silveira, T. L. Clarke, et al., "Assessing Kinetics and Recruitment of DNA Repair Factors Using High Content Screens," *Cell Reports* 37 (2021): 110176.

76. L. Gong, Y. Zhang, J. Zhao, et al., "All-In-One Biomimetic Nanoplatform Based on Hollow Polydopamine Nanoparticles for Synergistically Enhanced Radiotherapy of Colon Cancer," *Small* 18 (2022): 2107656.

77. X. Dong, R. Cheng, S. Zhu, et al., "A Heterojunction Structured $WO_{2.9}$-WSe_2 Nanoradiosensitizer Increases Local Tumor Ablation and Checkpoint Blockade Immunotherapy Upon Low Radiation Dose," *ACS Nano* 14 (2020): 5400–5416.

78. A. Gaudreau-Lapierre, D. Garneau, B. Djerir, F. Coulombe, T. Morin, and A. Marechal, "Investigation of Protein Recruitment to DNA Lesions Using 405 nm Laser Micro-Irradiation," *Journal of Visualized Experiments* 133 (2018): 57410, https://doi.org/10.3791/57410.

79. A. Gonzalez Rajal, K. A. Marzec, R. A. McCloy, et al., "A Non-Genetic, Cell Cycle-Dependent Mechanism of Platinum Resistance in Lung Adenocarcinoma," *Elife* 10 (2021): 65234.

80. X. Wang, C. Cao, X. Tan, et al., "SETD8, a Frequently Mutated Gene in Cervical Cancer, Enhances Cisplatin Sensitivity by Impairing DNA Repair," *Cell & Bioscience* 13 (2023): 107.

81. F. Chen, F. Ruan, X. Xie, et al., "Gold Nanocluster: A Photoelectric Converter for X-Ray-Activated Chemotherapy," *Advanced Materials* 36 (2024): 2402966.

82. N. Jackson, I. Hill, A. Alhussan, et al., "Dual Enhancement in the Radiosensitivity of Prostate Cancer Through Nanoparticles and Chemotherapeutics," *Cancer Nanotechnology* 14 (2023): 75.

83. B. Rubio-Ruiz, A. M. Pérez-López, L. Uson, et al., "In Cellulo Bioorthogonal Catalysis by Encapsulated AuPd Nanoalloys: Overcoming Intracellular Deactivation," *Nano Letters* 23 (2023): 804–811.

84. M. Sancho-Albero, M. Encinas-Gimenez, V. Sebastian, et al., "Transfer of Photothermal Nanoparticles Using Stem Cell Derived Small Extracellular Vesicles for In Vivo Treatment of Primary and Multinodular Tumours," *Journal of Extracellular Vesicles* 11 (2022): 12193.

85. M. M. Encabo-Berzosa, M. Gimeno, L. Lujan, et al., "Selective Delivery of Photothermal Nanoparticles to Tumors Using Mesenchymal Stem Cells as Trojan Horses," *RSC Advances* 6 (2016): 58723–58732.

86. Y. Yong, C. Zhang, Z. Gu, et al., "Polyoxometalate-Based Radiosensitization Platform for Treating Hypoxic Tumors by Attenuating Radioresistance and Enhancing Radiation Response," *ACS Nano* 11 (2017): 7164–7176.

87. L. Chen, M. Liu, Y. Wang, et al., "TME-Activated MnO_2/Pt Nanoplatform of Hydroxyl Radical and Oxygen Generation to Synergistically Promote Radiotherapy and MR Imaging of Glioblastoma," *International Journal of Nanomedicine* 19 (2024): 11055–11070.

88. X. Yi, L. Chen, X. Zhong, et al., "Core–Shell Au@MnO_2 Nanoparticles for Enhanced Radiotherapy via Improving the Tumor Oxygenation," *Nano Research* 9 (2016): 3267–3278.

89. P.-H. Tan, B.-H. Bay, G. Yip, et al., "Immunohistochemical Detection of Ki67 in Breast Cancer Correlates With Transcriptional Regulation of Genes Related to Apoptosis and Cell Death," *Modern Pathology* 18 (2005): 374–381.

90. T. N. Aung, B. Acs, J. Warrell, et al., "A New Tool for Technical Standardization of the Ki67 Immunohistochemical Assay," *Modern Pathology* 34 (2021): 1261–1270.

91. S. Wilhelm, A. J. Tavares, Q. Dai, et al., "Analysis of Nanoparticle Delivery to Tumours," *Nature Reviews Materials* 1 (2016): 16014.

92. N. A. P. Franken, H. M. Rodermond, J. Stap, J. Haveman, and C. van Bree, "Clonogenic Assay of Cells In Vitro," *Nature Protocols* 1 (2006): 2315–2319.

93. C. Borek, E. J. Hall, and M. Zaider, "X-Rays May Be Twice as Potent as γ Rays for Malignant Transformation at Low Doses," *Nature* 301 (1983): 156–158.

94. H. I. Amols, B. Lagueux, and D. Cagna, "Radiobiological Effectiveness (RBE) of Megavoltage X-Ray and Electron Beams in Radiotherapy," *Radiation Research* 105 (1986): 58–67.

Supporting Information

Additional supporting information can be found online in the Supporting Information section.

Supporting File: adfm75237-sup-0001-SuppMat.docx.